

# Nonlinear Incompressible Shear Wave Models in Hyperelasticity and Viscoelasticity Frameworks, with Applications to Love Waves

Shawn Samuel Carl McAdam<sup>\*1</sup>, Samuel Opoku Agyemang<sup>†1</sup>, and Alexei Cheviakov<sup>‡1</sup>

<sup>1</sup>Department of Mathematics and Statistics, University of Saskatchewan

March 20, 2026

## Abstract

General equations describing shear displacements in incompressible hyperelastic materials, holding for an arbitrary form of strain energy density function, are presented and applied to the description of nonlinear Love-type waves propagating on an interface between materials with different mechanical properties. The model is valid for a broad class of hyper-viscoelastic materials. For a cubic Yeoh model, shear wave equations contain cubic and quintic differential polynomial terms, including viscoelasticity contributions in terms of dispersion terms that include mixed derivatives  $u_{xxt}$  of the material displacement. Full (2+1)-dimensional numerical simulations of waves propagating in the bulk of a two-layered solid are undertaken and analyzed with respect to the source position and mechanical properties of the layers. Interfacial nonlinear Love waves and free upper surface shear waves are tracked; it is demonstrated that in the fully nonlinear case, the variable wave speed of interface and surface waves generally satisfies the linear Love wave existence condition  $c_1 < |v| < c_2$ , while tending to the larger material wave speed  $c_1$  or  $c_2$  for large times.

## 1 Introduction

The study of nonlinear shear waves propagating through an elastic material is fundamentally important in various areas of science and technology, including material sciences, seismology, geology, natural resource exploration, biological material research, and further medical applications. To briefly review, an elastic material resists external forces and returns to its original form when such forces are removed (unless the forces are too extreme, causing the material to yield and deform plastically). Commonly, models of elastic materials assume Hooke's law, where stress is linearly related to strain. This assumption holds for most materials undergoing small deformations, but neglects nonlinear effects in the stress-strain relation. The present work considers finite deformations of hyperelastic materials that possess a scalar strain energy density function  $W^H$  determining the stress-strain relationship (Section 3).

Materials such as polymers, rubbers, foams, and biological tissues exhibit essential nonlinear elastic behaviour when they undergo large elastic deformations. This nonlinear elastic behaviour under load or prescribed displacement can be modeled through a phenomenological approach [1], physical description approach [2], or use of experimental data [3]. The strain energy density is

---

<sup>\*</sup>Electronic mail: ssm259@usask.ca

<sup>†</sup>Electronic mail: soa964@usask.ca

<sup>‡</sup>Corresponding Author. Alternative English spelling: Alexey Shevyakov.  
Electronic mail: alexei.cheviakov@usask.ca

commonly either postulated from theoretical considerations or fitted in a certain form from experimental measurements. The form of the strain energy density is stated in terms of the deformation invariants such as principal stretches or matrix invariants of Cauchy-Green deformation tensors. In addition to hyperelastic behaviour, one may include viscoelastic constitutive model contributions through, for example, a pseudo-strain energy density function depending on the rate of change of a deformation tensor [4].

A major application area of linear elasticity theory is seismology. The fundamentals of seismic wave theory are built upon the seismic wave equation modelling a displacement  $\mathbf{u}(x^1, x^2, x^3) = (u^1, u^2, u^3)$  propagating through a linear, roughly isotropic material, such as Earth layers and geological formations:

$$\rho \frac{\partial^2 u^i}{\partial t^2} = (\lambda + \mu) \frac{\partial}{\partial x^i} \operatorname{div} \mathbf{u} + \mu \Delta u^i, \quad (1.1)$$

where the Lamé parameters  $\lambda, \mu > 0$  and the density  $\rho > 0$  may be assumed piecewise constant [5]. The seismic wave equation follows from the equations of motion of a continuum body and Hooke’s law for isotropic materials. Taking  $\lambda, \mu$ , and  $\rho$  to be piecewise constant allows one to model some of Earth’s anisotropy, typically as a stack of isotropic layers. The full seismic wave equation takes the Lamé parameters to be piecewise smooth functions of  $(x^1, x^2, x^3)$ , adding complexity to the equation. Using equation (1.1), one can determine that the divergence and curl of  $\mathbf{u}$  are described by D’Alembert’s equation (the linear wave equation) with wave speeds  $\sqrt{(\lambda + 2\mu)/\rho}$  and  $\sqrt{\mu/\rho}$  respectively. Compressional P–waves are solutions to the PDE for  $\operatorname{div} \mathbf{u}$  and transverse S–waves are solutions to the PDE for  $\operatorname{curl} \mathbf{u}$ . In particular, P–waves travel faster than S–waves.

P– and S–waves are body waves, and their energy decays as  $1/r^2$ , where  $r$  is the distance from the wave front to the focus of the initial displacement that caused them, such as an earthquake. Surface waves travel along the surface of the Earth at a slower rate than body waves, but preserve more of their energy, decaying as  $1/r$ . As such, surface waves dominate seismograms at large distances from an earthquake’s focus and cause a majority of the damage to human structures. One type of surface wave is the Love wave.

Love waves are horizontally polarized transverse waves, referred to as shear or SH-waves. Over large spatial scales (too large for the flat Earth approximation to apply), Love waves form from the interference of S–waves repeatedly reflecting off the slowly curving surface of the Earth [5]. A simplified model of Love waves considers two isotropic, homogeneous materials in the plane  $\mathbb{R}^2$ , that is, the flat-Earth model. The first material is represented by a horizontal strip of thickness  $L$ , and overlays the second material, occupying the space below a horizontal line, say  $z = 0$ . We refer to the line  $z = 0$  as the interface, and the line  $z = L$  as the surface. When the materials possess differing Young’s moduli, displacements between them travel at differing rates  $c_1$  and  $c_2$  respectively. Love waves are taken to be the waves that result from the interactions along the interface of the two media. Section 2 reviews this model in more detail, and includes an illustration of the domain (Figure 2.1).

In the fully linear case, it is known that Love waves only exist when  $c_1 < c_2$ , which we call the Love wave existence condition. The phase velocity  $v$  of a Love wave satisfies

$$c_1 < |v| < c_2. \quad (1.2)$$

Consequently, for shear waves propagating through linear elastic materials, the discontinuous wave speed determines the range of allowable phase velocities. If a seismic ray attempts to cross the interface but its angle of incidence is too large, then the ray is completely reflected (by Snell’s law). Such seismic rays are then trapped in the upper layer in perpetuity, making the upper layer a wave guide for seismic rays with large angles of incidence. If  $c_2 < c_1$ , such a reflection is impossible so every seismic ray eventually decays into the half space.

After assuming the appropriate conditions to use the flat Earth approximation (i.e. considering a rectangle with one face on the Earth’s surface and tens of kilometers deep), we may apply the above Love wave model with the continental crust as the upper layer, the solid uppermost mantle as the half-space, and the Mohorovičić (Moho) discontinuity as their interface. Below the oceanic floor, the Moho is consistently about 10 km deep. Below continental land mass, the Moho can range between 20 km and 70 km in depth, but averages about 40 km deep. We may consider the Moho to be of constant depth whenever the flat Earth approximation applies.

In the present work, we use continuum mechanics to derive an equation modelling nonlinear SH waves, that is, waves of finite amplitude, propagating through a hyperelastic, isotropic, incompressible, homogeneous, neo-Hookean material. The model generally allows for significant freedom through the choice of the constitutive strain energy density function  $W^H$  to approximate nonlinear stress-strain curves. We specialize the model to a particular strain energy density similar to those suggested in Murnaghan [6] and Bland [7]. The resulting model only requires a good approximation of the neo-Hookean material’s stress-strain curve with a cubic differential polynomial. Further, the model is a consequence of three necessary balance laws in a continuum body: conservation of mass and angular momentum, and the balance of linear momentum. The resulting model is given by the linear wave equation with cubic and quintic perturbations, and reduces to the linear model of SH waves for infinitesimal displacements. Further, our model includes the effects of energy dissipation through the use of a viscosity potential.

It is important to note that in modelling multiple shear wave settings, including earthquakes in particular, it is essential to consider finite displacements and resulting nonlinear PDEs. As verified in Bataille and Lund [8] the displacements and strains in earthquakes are small: the typical displacements caused by an earthquake ranges from  $10^{-10}$ m to  $10^{-1}$ m and typical earthquake strain of the ground ranges from  $10^{-6}$  to  $10^{-2}$ ; however, Bataille and Lund also argued that nonlinear effects should be included when modelling surface waves because such nonlinearities may balance out the dispersion effects in current linear Love wave models. Further, the displacements due to seismic waves are large near the focus of an earthquake. Because the flat Earth approximation is only valid over small spatial scales (hence, near the focus of the earthquake), our nonlinear model of SH waves is ideal for the flat Earth model of Love waves. Other applications include the description of shear waves in biological tissues and other complex materials (see, e.g., [9]).

The remainder of this paper is organized as follows. In Section 2, we review the Linear theory of Love waves and the corresponding solutions. In Section 3, we review the equations of motion and constitutive models of fully nonlinear hyperelastic bodies in the material (Lagrangian) framework. In Section 4, we derive a general partial differential equation model describing the propagation of one- and two-dimensional shear waves in incompressible hyperelastic materials for an arbitrary strain energy density function. In Section 5, we generalize the work in Section 4 to include viscoelastic effects. In particular, we derive the hyper-viscoelastic equation of motion satisfied by shear waves in the cubic Yeoh model framework. In Section 6, we numerically analyze the qualitative behaviour of solutions to the Love wave equation with finite displacements. In particular, wave fronts are efficiently tracked, and it is shown that, similar to the linear framework, the nonlinear Love-type wave speeds generally satisfy the inequality (1.2). In Section 7, we use symmetry methods to derive exact scaling-invariant solutions to our model in one spatial dimension. Though unbounded, with certain modifications, these solutions provide close agreement to the observed numerical behaviour.

## 2 Linear theory of Love waves

In two-dimensional space, consider an isotropic layer of height  $L$  overlying an isotropic elastic half-space and label their interface with the line  $z = 0$ . Let  $u = u(x, z, t)$  be a displacement perpendicular to this space at the point  $(x, z)$  and time  $t$ . Suppose the displacement  $u$  propagates through the space according to the following variation of the linear wave equation

$$u_{tt} = c(z)^2 (u_{xx} + u_{zz}), \quad c(z) = \begin{cases} c_1 & \text{if } 0 \leq z < L, \\ c_2 & \text{if } z < 0. \end{cases} \quad (2.1)$$

where subscripts denote partial differentiation whenever appropriate. We refer to equation (2.1) with piecewise constant wave speed as the linear Love wave equation. This equation models materials whose elements have a linear restoring force resulting from Hooke's law. The wave speed  $c^2$  is taken to be a piecewise-constant function of  $z$  because the speed of propagation depends on various properties of the two media. Love waves will propagate between the interface and the upper boundary  $z = L$  (which we refer to as the surface of this domain). The surface is stress-free, corresponding to a Neumann boundary condition  $u_z(x, L, t) = 0$ . At  $z \rightarrow -\infty$ ,  $u \rightarrow 0$  is assumed. Figure 2.1 illustrates this model.

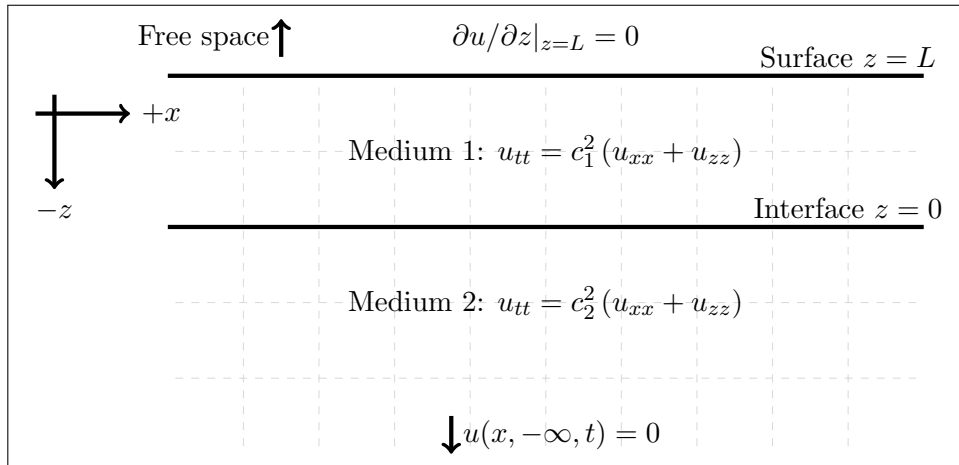


**Figure 2.1:** An isotropic layer overlying an isotropic elastic half-space. The  $y$  direction is perpendicular to this space spanned by  $x, z$ . The positive  $z$  direction points downwards,  $L$  is the depth of the isotropic layer, waves travelling through the isotropic layer (medium 1) have speed  $c_1^2$ , and waves travelling through the isotropic elastic half-space (medium 2) have speed  $c_2^2$ .

Commonly, one solves this problem by assuming that for fixed  $z$ , a Love wave has the form of a plane wave travelling along the  $x$  direction [10],

$$u(x, z, t) = f(z)e^{ik(x-vt)}, \quad (2.2)$$

where  $k$  is the wave number,  $v$  is the phase velocity of the wave, and  $f$  is some continuously differentiable function of the depth  $z$ . Here we aim to solve for  $f$  and find an expression for  $k$  as a function of  $v$ . Note that for (2.2) to represent a Love wave,  $f$  must decay exponentially as  $z \rightarrow -\infty$ . Further, observe that the phase velocity is assumed to not depend on depth  $z$ . Substituting (2.2) into the piecewise linear wave equation implies

$$f''(z) = k^2(1 - (v/c(z))^2)f(z) = \begin{cases} k^2(1 - (v/c_1)^2)f(z) & \text{if } 0 \leq z < L, \\ k^2(1 - (v/c_2)^2)f(z) & \text{if } z < 0, \end{cases} \quad (2.3)$$

and the boundary conditions imply  $f'(L) = f(-\infty) = 0$ . For any fixed value of  $v$ , equation (2.3) becomes a Sturm–Liouville boundary value problem (BVP)

$$(p(z)f'(z))' + q(z)f(z) = -\lambda r(z)f(z),$$

where  $p = 1, q = 0, \lambda = k^2$ , and  $r(z) = 1 - (v/c(z))^2$ . Recall that for an Sturm–Liouville BVP to be *regular*, the weight function  $r(z)$  must be a positive, continuous function over its domain. The ODE in equation (2.3) is *irregular* because  $r(z)$  is discontinuous at 0.

For every  $|v| \in (c_1, c_2)$  and every  $n \in \mathbb{Z}$ , the following is a countable set of eigenvalue/function pairs  $(k_n(v), f_n(z; v))$  for the above Sturm–Liouville BVP:

$$f_n(z; v) = \begin{cases} \cos(k_n(v)\Omega_1(v)(z - L)) & 0 \leq z < L, \\ \cos(k_n(v)\Omega_1(v)L)e^{k_n(v)|\Omega_2(v)z} & z < 0, \end{cases} \quad (2.4)$$

where

$$\Omega_1(v) = \sqrt{(v/c_1)^2 - 1}, \quad \Omega_2(v) = \sqrt{1 - (v/c_2)^2}.$$

The derivative  $f'_n(z; v)$  must be continuous at  $L$ , so  $\Omega_1(v)$  and  $\Omega_2(v)$  are related by

$$\Omega_2(v) = \text{sign}(k_n(v))\Omega_1(v) \tan(k_n(v)\Omega_1(v)L). \quad (2.5)$$

Both functions  $\Omega_1(v), \Omega_2(v)$  must output nonnegative real numbers for the solution  $f_n$  to satisfy the boundary conditions and be continuously differentiable at the interface  $z = 0$ . This determines the range of allowable phase velocities  $v$ , also called the *Love wave existence condition* (1.2):

$$c_1 < |v| < c_2. \quad (2.6)$$

The Love wave existence condition also implies the weight function  $r(z) \leq 0$  for  $z \in [0, L)$ , which is another reason why the Sturm–Liouville BVP (2.3) is not regular.

One can use equation (2.5) to solve for each eigenvalue  $k_n(v)$ ,

$$\begin{aligned} k_n(v) &= \frac{1}{L\Omega_1(v)} (\text{sign}(n) \arctan(\Omega_2(v)/\Omega_1(v)) + \pi n) \\ &= \frac{c_1}{L\sqrt{v^2 - c_1^2}} \left( \text{sign}(n) \arctan \left( \frac{c_1}{c_2} \sqrt{\frac{c_2^2 - v^2}{v^2 - c_1^2}} \right) + \pi n \right) \\ &= \text{sign}(n)k_0(v) + \frac{\pi n}{L\Omega_1(v)}. \end{aligned}$$

Because  $k_0(v)$  is nonzero, there are two distinct eigenvalues  $\pm k_0(v)$  corresponding to 0, which we label with  $\pm k_{\pm 0}(v) = k_{\pm 0}(v)$ . We observe that  $k_{-n}(v) = -k_n(v)$  for every  $n$  (including  $n = 0$ ) so the eigenfunctions satisfy  $f_{-n}(z, v) = f_n(z, v)$ . Each eigenfunction then corresponds to two distinct eigenvalues  $\pm k_n(v)$ . The negative  $n$  eigenfunctions do not yield new linearly independent solutions; however, the overall solution mode  $f_n(z, v)e^{ik_n(v)(x-vt)}$  *does* change. Now that we have an equation for  $k_n$ , we see that the inequalities are strict in (1.2) because  $f_n(z, c_2) = (-1)^n$  for  $z < 0$  (hence does not decay as  $z \rightarrow -\infty$ ) and  $f_n(z, c_1)$  is not continuously differentiable at  $z = 0$ . Indeed,  $f_n(z, c_1) = 0$  for  $z \leq 0$  (because  $k_n$  has a pole at  $c_1$ ) and  $\partial_z f_n(z, c_1)|_{z=0^+} = -k_n(c_1)\Omega_1(c_1) \sin(k_n(c_1)\Omega_1(c_1)L) \neq 0$ .

There is a countably infinite set of wave numbers  $k_n(v)$  corresponding to a given phase velocity  $v$ . We note that  $k_n(v), \Omega_1(v), \Omega_2(v)$ , and  $f_n(z; v)$  are all *even* with respect to  $v$ , so we need only study these function for positive  $v$ . Each  $k_n(v)$  is a strictly decreasing function of  $v \in (c_1, c_2)$

for  $n \geq 0$  because  $\Omega_1(v)$  strictly increases,  $\Omega_2(v)/\Omega_1(v)$  strictly decreases, and arctan strictly increases. As such,  $k_n(v)$  realizes its minimum at  $v = c_2$  and we have the following lower bound on each  $k_n(v)$ ,

$$k_n(v) \geq k_0(c_2) + \frac{\pi n}{L\Omega_1(c_2)} \geq n \frac{\pi c_1}{L\sqrt{c_2^2 - c_1^2}}.$$

This result implies there are finitely many phase velocities  $v$  corresponding to a given wave number  $k^*$ . Further,  $k_n$  restricted to  $[c_1, c_2]$  is invertible and its inverse has the domain  $[n\pi c_1 / L\sqrt{c_2^2 - c_1^2}, \text{sign}(n)\infty]$ .

Figure 2.2 plots  $f_n(z; v')$  for  $x \in [0, 3L]$  with  $v' = (c_1 + c_2)/2$ , and  $k_n(v)$  for  $v \in [c_1, c_2]$  both for various values of  $n$ . Increasing  $n$  by 1 increases  $k_n(v)$  by  $\pi/(L\Omega_1(v))$ . This has the effect of increasing the frequency of oscillations of  $f_n(z; v)$  for  $z \in [0, L]$ , and makes  $f_n(z; v)$  decay faster for  $z \geq L$ . Increasing  $n$  also makes  $u(x, z, t) = f_n(z; v)e^{ik_n(v)(x-vt)}$  oscillate more along the  $x$  direction. This is illustrated in Figure 2.3 which contains plots of fundamental solutions to equation (2.1) for various  $n$  and  $v$ .

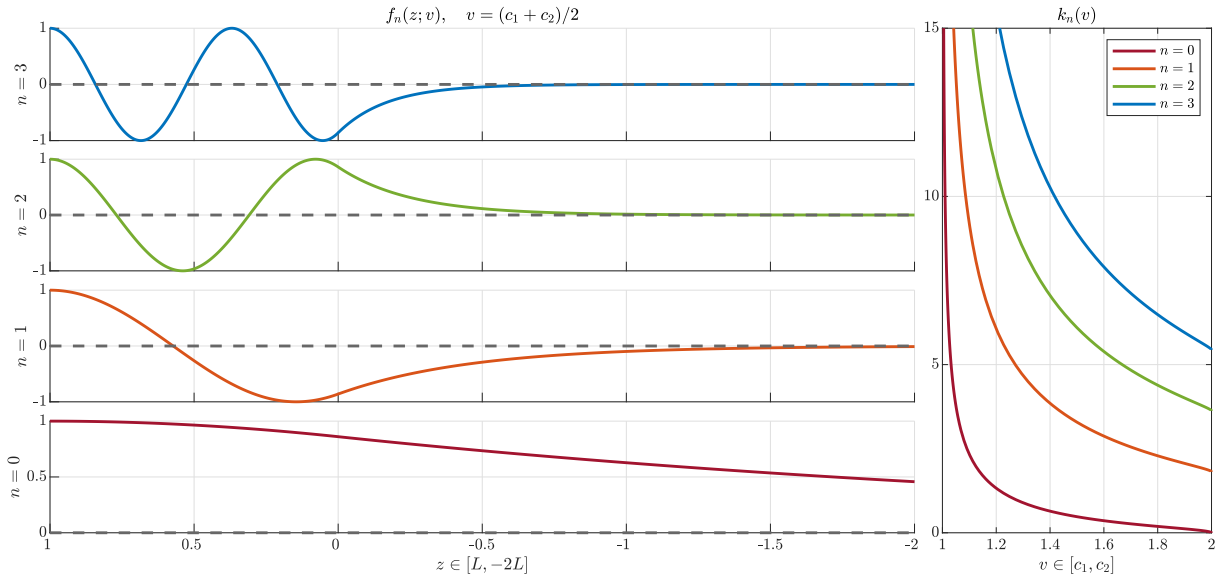


**Figure 2.2:** Left: plots of  $f_0(z; v)$ ,  $f_1(z; v)$ ,  $f_2(z; v)$ , and  $f_3(z; v)$  for  $z \in [0, 3L]$  and  $v = (c_1 + c_2)/2$ . Right: plot of  $k_n(v)$  over  $v \in [c_1, c_2]$  for  $n = 0, 1, 2, 3$ . Recall that  $k_n(v)$  strictly increases with  $n$ . Other parameters are  $L = 1$ ,  $c_1 = 1$ ,  $c_2 = 2$

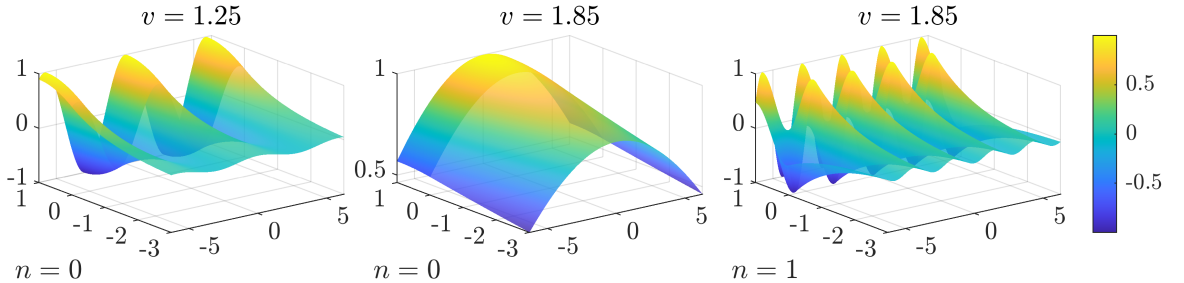


**Figure 2.3:** The real part of fundamental solutions  $f_n(z; v)e^{ik_n(v)(x-vt)}$  to equation (2.1) for various  $v$  and  $n$ , with  $c_1 = 1$ ,  $c_2 = 2$ , and  $L = 1$ .

A solution of the form  $f_n(z; v)e^{ik_n(v)(x-vt)}$  exists for each  $|v| \in (c_1, c_2)$  and each  $n \in \mathbb{Z}$ . Let  $\mathcal{D} = (-c_2, -c_1) \cup (c_1, c_2)$ , then the most general plane wave solution to the linear Love wave

equation (2.1) is of the form

$$u(x, z, t) = \sum_{n=-\infty}^{\infty} \int_{\mathcal{D}} \alpha_n(v) f_n(z; v) e^{ik_n(v)(x-vt)} dv \quad (2.7)$$

where we recall that the solution corresponding to  $n = 0$  is counted twice in the first line because there are two distinct 0<sup>th</sup> modes with eigenvalues  $\pm k_0(v)$ .

We determine the coefficients  $\alpha_n(v)$  from sufficiently smooth initial conditions  $u(x, z, 0) = F(x, z)$  and  $u_t(x, z, 0) = G(x, z)$ . Because  $f_n$  and  $k_n$  are even over  $v$ , we have

$$F(x, z) = \sum_{n=-\infty}^{\infty} \int_{c_1}^{c_2} (\alpha_n(v) + \alpha_n(-v)) f_n(z; v) e^{ik_n(v)x} dv. \quad (2.8)$$

We can write this as an inverse Fourier transform by substituting  $w = k_n(v)$ . We observe that the bounds on each integral now depend on  $n$  as shown in the following. Let  $b_n = |n|\pi c_1 / L\sqrt{c_2^2 - c_1^2}$ , then

$$\begin{aligned} F(x, z) = & - \sum_{n=0}^{\infty} \int_{b_n}^{\infty} \frac{[\alpha_n(k_n^{-1}(w)) + \alpha_n(-k_n^{-1}(w))]}{k'_n(k_n^{-1}(w))} f_n(z; k_n^{-1}(w)) e^{iwx} dw \\ & + \sum_{n=0}^{\infty} \int_{-\infty}^{-b_n} \frac{[\alpha_{-n}(k_{-n}^{-1}(w)) + \alpha_{-n}(-k_{-n}^{-1}(w))]}{k'_{-n}(k_{-n}^{-1}(w))} f_n(z; k_{-n}^{-1}(w)) e^{iwx} dw. \end{aligned}$$

We can significantly simplify this integral by defining the sequence  $A_0, A_1, \dots$  of piecewise functions,

$$A_n(w) = \begin{cases} \alpha_n(k_n^{-1}(w)) + \alpha_n(-k_n^{-1}(w)) & \text{if } w \geq b_n, \\ \alpha_{-n}(k_{-n}^{-1}(w)) + \alpha_{-n}(-k_{-n}^{-1}(w)) & \text{if } w \leq -b_n, \\ 0 & \text{otherwise.} \end{cases}$$

Further,  $k_{-n}(v) = -k_n(v)$ , so we have  $k_{-n}^{-1}(w) = k_n^{-1}(-w)$ . In total,

$$F(x, z) = - \int_{-\infty}^{\infty} e^{iwx} \sum_{n=0}^{\infty} \frac{A_n(w)}{k'_n(k_n^{-1}(|w|))} f_n(z; k_n^{-1}(|w|)) dw,$$

and applying the inverse Fourier transform to both sides results in

$$\frac{1}{2\pi} \int_{-\infty}^{\infty} F(x, z) e^{-iwx} dx = - \sum_{n=0}^{\infty} \frac{A_n(w)}{k'_n(k_n^{-1}(|w|))} f_n(z; k_n^{-1}(|w|)).$$

The eigenfunctions from (2.3) are orthogonal with respect to the weight function  $r(z; v) = 1 - (v/c(z))^2$ . They satisfy the equation

$$\int_{-\infty}^L f_n(z; v) f_m(z; v) r(z; v) dz = \begin{cases} -\frac{L}{2} \Omega_1(v)^2 & \text{if } |m| = |n|, \\ 0 & \text{otherwise,} \end{cases}$$

where the minus sign appears in the  $r$ -norm because  $r(z; v) < 0$  for  $0 \leq z < L$ . With this, we isolate for each term in the summation above by multiplying each side by  $f_n(z; k_n^{-1}(|w|)) r(z; k_n^{-1}(|w|))$  and integrating over  $z$ . The resulting formula for each  $A_n(w)$  is,

$$A_n(w) = \frac{k'_n(k_n^{-1}(|w|))}{\pi L \Omega_1(k_n^{-1}(|w|))^2} \int_{-\infty}^L \int_{-\infty}^{\infty} F(x, z) f_n(z; k_n^{-1}(|w|)) r(z; k_n^{-1}(|w|)) e^{-iwx} dx dz$$

With this, we are halfway to solving for each  $\alpha_n(v)$  because,

$$\begin{aligned} A_n(\pm k_n(v)) &= \frac{k'_n(v)}{\pi L \Omega_1(v)^2} \int_{-\infty}^L \int_{-\infty}^{\infty} F(x, z) f_n(z; v) r(z; v) e^{\mp i k_n(v) x} dx dz \\ &= \alpha_{\pm n}(v) + \alpha_{\pm n}(-v), \quad n \geq 0. \end{aligned}$$

With the initial condition for  $u_t(x, z, 0) = G(x, z)$  and the same logic as presented above, we compute a similar formula for the difference between two coefficients,

$$\pm(\alpha_{\pm n}(v) - \alpha_{\pm n}(-v)) = \frac{i k'_n(v)}{\pi L \Omega_1(v)^2 v k_n(v)} \int_{-\infty}^L \int_{-\infty}^{\infty} G(x, z) f_n(z; v) r(z; v) e^{\mp i k_n(v) x} dx dz.$$

For our purposes, we only consider  $u_t(x, z, 0) = 0$ , so  $\alpha_n(v) = \alpha_n(-v)$ ,  $\alpha_{-n}(v) = \overline{\alpha_n(v)}$ , and the solution takes the form

$$u(x, z, t) = 4 \sum_{n=0}^{\infty} \int_{c_1}^{c_2} f_n(z; v) \cos(k_n(v)vt) \operatorname{Re} \left( \alpha_n(v) e^{i k_n(v)x} \right) dv.$$

Implicit in the assumption (2.2) is that the phase does not change with depth  $z$ . This assumption is carried through to Equation (2.7). As a consequence of this assumption and the fact that the Sturm-Liouville problem (2.3) is not regular, the set of eigenfunctions  $\{f_n\}$  is not complete. The decomposition (2.8) holds only for a subset of initial conditions of the problem for (2.1).

In Section 6.2, we use the method of lines to numerically study the initial behaviour of linear and nonlinear Love waves subject to a sudden explosion. While doing so, we record the velocity of the waves travelling horizontally along the surface and interface. We find that these velocities initially differ, but eventually take on the same value. As such, the solution we derived can describe sufficiently large-time behaviour of a Love wave moving along the  $x$  direction.

### 3 Nonlinear hyperelasticity and constitutive models

The hyperelasticity framework provides a natural generalization of linear waves corresponding to small displacements in nonlinear materials, including geological formations, to the case where displacements are not small. In this section, we describe the behaviour of incompressible hyperelastic media undergoing finite (possibly large) strains when subjected to external stress. We briefly recall the notation and the main ingredients of mathematical models in incompressible hyperelasticity required for this study (see, e.g., Refs. [11–14] for full details). Vectors and tensors are indicated with boldface characters and their entries are written in italics. Entries of vectors and tensors are written in italics, and summation in repeated indices is assumed where appropriate. We use Cartesian coordinates and the flat space metric  $g^{ij} = \delta^{ij}$ .

#### 3.1 Hyperelastic materials: equations of motion

Consider an elastic solid parameterized by material (Lagrangian) coordinates  $\mathbf{X} = (X, Y, Z) = (X^1, X^2, X^3)$  in a spatial region  $\bar{\Omega}_0 \subset \mathbb{R}^3$  with a piecewise-smooth boundary. We call  $\bar{\Omega}_0$  the reference configuration or the natural state of the solid. After deformations, the actual shape of the solid at time  $t$  is given by the time-dependent Eulerian coordinates  $\mathbf{x} = (x, y, z) = (x^1, x^2, x^3)$  in the actual configuration  $\bar{\Omega} \subset \mathbb{R}^3$ . The Eulerian coordinates can be interpreted as an invertible, smooth, orientation-preserving map deforming the body over time,

$$\mathbf{x} = \mathbf{x}(\mathbf{X}, t) = \mathbf{X} + \mathbf{u}(\mathbf{X}, t). \tag{3.1}$$

The map  $\mathbf{x}$  is also referred to as a deformation field.  $\mathbf{u} = \mathbf{u}(\mathbf{X}, t)$  has the meaning of displacement and is not assumed to be small. Figure 3.1 illustrates this situation along with area elements, the normal vector  $\mathbf{N}$  about a point  $\mathbf{X}$  in the reference configuration, and its corresponding normal vector  $\mathbf{n}$  point  $\mathbf{x}$  in the actual configuration. The velocity and the acceleration of a material point  $\mathbf{X}$  are given by  $\mathbf{v}(\mathbf{X}, t) = \partial\mathbf{x}/\partial t$  and  $\mathbf{a}(\mathbf{X}, t) = \partial^2\mathbf{x}/\partial t^2$ . We aim to describe a system of PDEs describing the deformation field  $\mathbf{x}$  in terms of its derivatives in  $\mathbf{X}$  and  $t$ .

The deformation gradient  $\mathbf{F}$  is the Jacobian of  $\mathbf{x}$  with respect to  $\mathbf{X}$ ,

$$\mathbf{F}(\mathbf{X}, t) = \text{grad}_{\mathbf{X}}\mathbf{x}, \quad F_j^i = \frac{\partial x^i}{\partial X^j}. \quad (3.2)$$

Because  $\mathbf{x}$  is an orientation-preserving map,  $J \equiv \det(\mathbf{F}) > 0$ . The map  $\mathbf{x}$  preserves volumes for incompressible materials, so  $J = 1$ . We note that when reasonable, we write formulae in terms of general  $J$ , and then substitute  $J = 1$ . If the density of the elastic material in the Lagrange configuration is represented by  $\rho_0 = \rho_0(\mathbf{X})$ , the current time-dependent mass density in Lagrangian coordinates takes the form

$$\rho(\mathbf{X}, t) = \rho_0(\mathbf{X})/J = \rho_0(\mathbf{X}).$$

The left and right Cauchy-Green deformation tensors  $\mathbf{B} = \mathbf{F}\mathbf{F}^T$  and  $\mathbf{C} = \mathbf{F}^T\mathbf{F}$  play an essential role in the formulation of the equations of motion in solid mechanics. For our purposes, we regard  $\mathbf{B}$  and  $\mathbf{C}$  as matrices to avoid unnecessary tensor algebra.  $\mathbf{B}$  and  $\mathbf{C}$  are symmetric positive-definite and share the same set of eigenvalues. The square roots of these eigenvalues determine the singular values  $(\sigma_1, \sigma_2, \sigma_3)$  of  $\mathbf{F}$  which are referred to as the principal stretches.

Let  $\mathbf{t}$  be the traction vector representing force per unit area acting on the area element  $da$  with unit normal vector  $\mathbf{n}$  in the actual configuration. According to the Cauchy theorem,  $\mathbf{t} = \boldsymbol{\sigma}\mathbf{n}$ , where  $\boldsymbol{\sigma} = \boldsymbol{\sigma}(\mathbf{x}, t)$  is the symmetric Cauchy stress tensor. Let  $\mathbf{T}$  be the corresponding traction vector in the reference configuration acting on the undeformed area element  $dA$  with unit normal vector  $\mathbf{N}$ .  $\mathbf{T}$  is given by  $\mathbf{T} = \mathbf{P}\mathbf{N}$ , where  $\mathbf{P} = \mathbf{P}(\mathbf{X}, t)$  denotes the asymmetric first Piola-Kirchhoff stress tensor, related to the Cauchy stress through  $\mathbf{P} = J\boldsymbol{\sigma}\mathbf{F}^{-T}$ . Here  $\mathbf{F}^{-T}$  is the inverse of the transpose of  $\mathbf{F}$ . The equations of motion of  $\mathbf{x}$  are given directly in terms of  $\mathbf{P}$ . The second Piola-Kirchhoff stress tensor  $\mathbf{S}$  is given in terms of the deformation gradient  $\mathbf{F}$  and the first Piola-Kirchhoff stress tensor  $\mathbf{P}$  by  $\mathbf{S} = \mathbf{F}^{-1}\mathbf{P}$ .

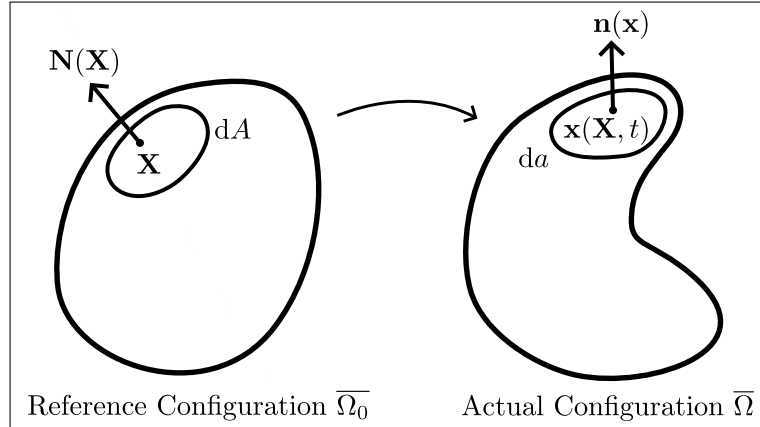


**Figure 3.1:** A general illustration of the deformation  $\mathbf{x}(\mathbf{X}, t)$  acting on the reference configuration after some time  $t$ .

The stress tensors  $\mathbf{P}$  and  $\mathbf{S}$  can be explicitly determined by assuming the form of  $\mathbf{x}$  (e.g. through specification of variables  $X^1, X^2$ , or  $X^3$  or their combinations that  $x^1, x^2$ , or  $x^3$  depend on) and a scalar-valued volumetric hyperelastic strain energy density  $W^H = W^H(\mathbf{X}, \mathbf{F})$

(sometimes called stored energy density function). In the incompressible hyperelasticity framework, the Piola-Kirchhoff stress tensors are determined by the strain energy density through the formulas

$$\mathbf{P} = -p\mathbf{F}^{-T} + \rho_0 \frac{\partial W^H}{\partial \mathbf{F}} = \mathbf{F}\mathbf{S}, \quad \mathbf{S} = -p\mathbf{C}^{-1} + 2\rho_0 \frac{\partial W^H}{\partial \mathbf{C}}, \quad (3.3)$$

where  $p = p(\mathbf{X}, t)$  denotes hydrostatic pressure. Partial derivatives taken with respect to a matrix/tensor are interpreted as a symmetrized partial derivative with respect to each entry of the matrix/tensor. For example, the entries of  $\partial W^H / \partial \mathbf{C}$  are given by

$$\left( \frac{\partial W^H}{\partial \mathbf{C}} \right)_{ij} = \frac{1}{2} \left( \frac{\partial W^H}{\partial C^{ij}} + \frac{\partial W^H}{\partial C^{ji}} \right). \quad (3.4)$$

For isotropic, homogenous, frame-indifferent, hyperelastic media, the strain energy density function can be written as a function of the three principal invariants  $I_1$ ,  $I_2$ , and  $I_3$  of the Cauchy-Green deformation tensors  $\mathbf{B}$  and  $\mathbf{C}$

$$W^H = W_{\text{iso}}^H(I_1, I_2, I_3). \quad (3.5)$$

The principal invariants are the coefficients of the characteristic polynomial of  $\mathbf{B}$ ,

$$I_1 = \text{tr}(\mathbf{B}), \quad I_2 = \frac{1}{2} (I_1^2 - \text{tr}(\mathbf{B}^2)), \quad I_3 = \det(\mathbf{B}) = J^2. \quad (3.6)$$

Generally, a set of invariants can be any independent combination of principal stretches (meaning they cannot be written in terms of the other invariants). Because  $\mathbf{x}$  preserves volumes (i.e.  $I_3 = J^2 = 1$ ), the strain energy density has a simpler form  $W^H = W^H(I_1, I_2)$ . We note that when modelling anisotropic materials,  $W^H$  additionally depends on direction of anisotropy, such as the direction of embedded fibers, through additional invariants (see, e.g., [9, 11, 12] and references therein).

The formulae for  $W^H$  only involve its partial derivatives, so we may choose the constant term. Observe that in the natural state  $\mathbf{x} = \mathbf{X}$ , the deformation gradient  $\mathbf{F} = \mathbf{I}$  is the identity matrix, and  $I_1 = I_2 = n$  in  $n$  dimensions. In three dimensions, it is common to take

$$W^H = W^H(I_1 - 3, I_2 - 3). \quad (3.7)$$

We may then take  $W^H(0, 0) = 0$  in the natural state.

The following are examples of strain energy density functions. Mooney-Rivlin solids obey the following strain energy density function

$$W^H = a(I_1 - 3) + b(I_2 - 3), \quad (3.8)$$

where  $a, b \geq 0$  are constant parameters. Any incompressible, lubber-like material is a Mooney-Rivlin solid. For  $b = 0$ , (3.8) reduces to the strain energy density function of a neo-Hookean material

$$W^H = a(I_1 - 3).$$

The linear wave equation is the equation of motion for shear waves travelling through a neo-Hookean solid. There are generalized version of both the Mooney-Rivlin and neo-Hookean models. The generalized Mooney-Rivlin function is a bivariate polynomial in  $I_1 - 3$  and  $I_2 - 3$ ,

$$W^H = \sum_{i=0}^k \sum_{j=0}^l c_{ij} (I_1 - 3)^i (I_2 - 3)^j, \quad (3.9)$$

where  $c_{ij}$  are constant material coefficients with  $c_{00} = 0$ . These model what are called polynomial-type materials [15]. One such generalized Mooney-Rivlin function is the Murnaghan potential. In a two-dimensional setting, the Murnaghan potential has been recently employed in Ref. [16] to derive a weakly nonlinear analog of the *Love hypothesis* (which relates the radial displacement and the longitudinal strain) for a wave propagation model in an elastic rod undergoing shear and longitudinal axially symmetric displacements.

The generalized neo-Hookean model takes the strain energy density function to be any function of  $I_1 - 3$  without a dependence on  $I_2 - 3$ ,

$$W^H = W^H(I_1 - 3).$$

Much of the following is restricted to generalized neo-Hookean materials because allowing  $W^H$  to depend on  $I_2$  significantly complicates the equations of motion. We apply the results of the following section to a Yeoh model [17]

$$W^H = \sum_{i=0}^k c_i (I_1 - 3)^i, \quad (3.10)$$

with  $k = 3$ , resulting in the polynomial

$$W^H = \mu(I_1 - 3) + \frac{1}{2}M(I_1 - 3)^2 + \frac{1}{3}A(I_1 - 3)^3, \quad (3.11)$$

where  $\mu, M, A$  are constants. For theoretical reasons explained shortly, it is also desirable for  $W^H$  to be a convex polynomial. The coefficients of the above polynomial models can be fit to a given material's stress-strain curve. Further generalizations to the above strain energy density functions are possible and can be found in, e.g., [18, 19]. These are useful if a material's stress-strain curve does not accurately fit to the above forms.

It is desirable for the strain energy density function to be *polyconvex*. This is the case for generalized Mooney-Rivlin functions (and their specializations) whenever  $c_{ij} \geq 0$  for each  $i, j$  [11]. Models built from a polyconvex strain energy density function have the following three desirable properties. First, increasing the strain increases the elastic energy. Second, the natural state corresponds to a stable equilibrium. Lastly, polyconvexity guarantees the existence of solutions of boundary value problems in linear elasticity [20]. Many realistic materials possess the first two properties, so they should be modelled by polyconvex strain energy density functions. The last property is desirable in practice.

To provide the mathematical definition of polyconvexity, a real valued function  $G = G(\mathbf{F})$  of 3 by 3 tensors is polyconvex if it can be written as

$$G(\mathbf{F}) = g(\mathbf{F}, \text{cof}\mathbf{F}, \det \mathbf{F})$$

where  $g$  is a (typically nonunique) convex function of the entries of  $\mathbf{F}$ ,  $\mathbf{F}$ 's matrix of cofactors  $\text{cof}\mathbf{F}$ , and  $\det \mathbf{F}$  [12]. For the examples, suppose  $h: \mathbb{R} \rightarrow \mathbb{R}$  is convex. Any function of the form  $G(\mathbf{F}) = h(\det \mathbf{F})$  is polyconvex but not necessarily convex with respect to the entries of  $\mathbf{F}$ . Further,  $G(\mathbf{F}) = h(|\mathbf{F}|)$  where  $|\mathbf{F}|$  denotes the Frobenius norm of  $\mathbf{F}$  is both polyconvex and convex with respect to the entries of  $\mathbf{F}$ .

The full system of equations of motion for incompressible hyperelastic materials in three dimensions is given by

$$\rho_0 \frac{\partial^2 \mathbf{x}}{\partial t^2} = \text{div}_{\mathbf{x}} \mathbf{P} + \mathbf{D}_f, \quad (3.12a)$$

$$\mathbf{P}\mathbf{F}^T = \mathbf{F}\mathbf{P}^T, \quad (3.12b)$$

$$J = \det(\mathbf{F}) = 1, \quad (3.12c)$$

where  $\mathbf{D}_f$  are the body forces per unit volume (e.g. gravity). The  $i^{\text{th}}$  component of the divergence of the tensor  $\mathbf{P}$  with respect to the Lagrangian coordinates  $\mathbf{X}$  is the divergence of the  $i^{\text{th}}$  row of  $\mathbf{P}$ . So,

$$(\text{div}_{\mathbf{X}}\mathbf{P})^i = \text{div}_{\mathbf{X}}(\mathbf{P}^i) = \frac{\partial}{\partial X^j} P_j^i.$$

The equations of motion are a result of three practical balance laws (conservation of mass and angular momentum, and balance of linear momentum). The balance law (3.12a) is known as the momentum equation. Equation (3.12a) expresses a conservation law if  $\mathbf{D}_f = 0$ , where it becomes a total divergence. The condition (3.12b) expresses conservation of angular momentum and is equivalent to requiring the Cauchy stress tensor be symmetric  $\boldsymbol{\sigma} = \boldsymbol{\sigma}^T$ . For isotropic materials, as well as in some other cases, this symmetry condition is identically satisfied (e.g., Ref. [19]).

To summarize (and provide a preview of the following), one can use equation 3.12 to model an incompressible hyperelastic material after assuming the form of  $\mathbf{x}$ , fitting a strain energy density function  $W^H$  to their material's stress-strain curve, and then finding the first Piola-Kirchhoff stress tensor. This process is made easier when the material is isotropic, homogenous and frame-indifferent because then  $W^H$  is a function of three arguments (the principal invariants of  $\mathbf{B} = \mathbf{F}\mathbf{F}^T$ ). In that case, one can assume a general form for  $W^H$ , then the PDE (3.12a) will model any material whose stress-strain curve is well approximated by such  $W^H$ .

## 4 Nonlinear hyperelastic shear waves

### 4.1 The general wave equation for an arbitrary strain energy density function

Consider a shear wave with displacements in the  $Y$ -direction propagating through the  $X - Z$  plane (which is antiplane motion) described by

$$\mathbf{x} = \begin{bmatrix} x \\ y \\ z \end{bmatrix} = \begin{bmatrix} X \\ Y \\ Z \end{bmatrix} + \begin{bmatrix} 0 \\ v(t, X, Z) \\ 0 \end{bmatrix}. \quad (4.1)$$

Our aim is to derive the equations of motion for  $v(X, Z, t)$ . As discussed in Section 3, these follow from computing  $\mathbf{P}$ . The deformation gradient and its inverse are

$$\mathbf{F} = \begin{bmatrix} 1 & 0 & 0 \\ v_X & 1 & v_Z \\ 0 & 0 & 1 \end{bmatrix}, \quad \mathbf{F}^{-1} = \begin{bmatrix} 1 & 0 & 0 \\ -v_X & 1 & -v_Z \\ 0 & 0 & 1 \end{bmatrix}, \quad (4.2)$$

where  $v_X = \partial v / \partial X$ , and  $v_Z = \partial v / \partial Z$  represent the amount of shear. The left and right Cauchy-Green deformation tensors  $\mathbf{B}$  and  $\mathbf{C}$  are

$$\mathbf{C} = \begin{bmatrix} 1 + v_X^2 & v_X & v_X v_Z \\ v_X & 1 & v_Z \\ v_X v_Z & v_Z & 1 + v_Z^2 \end{bmatrix}, \quad \mathbf{B} = \begin{bmatrix} 1 & v_X & 0 \\ v_X & v_X^2 + v_Z^2 + 1 & v_Z \\ 0 & v_Z & 1 \end{bmatrix}. \quad (4.3)$$

The principal invariants for the deformation field (4.1) are

$$I_1 = I_2 = 3 + v_X^2 + v_Z^2 = 3 + \|\text{grad } v\|^2 = |\mathbf{F}|^2, \quad I_3 = 1.$$

where  $|\mathbf{F}|$  is the Frobenius norm of  $\mathbf{F}$ . The shear displacements (4.1) are naturally incompressible because  $I_3 = \det(\mathbf{F}) = 1$ . It is important to note that, although  $I_1 = I_2$ , we cannot use this

fact until after expanding (3.3) and (3.4). Doing otherwise would miss a necessary condition to ensure the pressure is well defined.

Equation (3.3) yields the first Piola-Kirchhoff stress tensor

$$\mathbf{P} = -p\mathbf{F}^{-T} + 2W_1^H\mathbf{F} - 2W_2^H\mathbf{B}^{-1}\mathbf{F}^{-T}, \quad (4.4)$$

where  $W^H = W^H(I_1, I_2)$ ,  $W_1^H \equiv \frac{\partial W^H}{\partial I_1}$ ,  $W_2^H \equiv \frac{\partial W^H}{\partial I_2}$ , and  $p = p(X, Z, t)$ . Substituting (4.4) into the equations of motion (3.12a) yield the following system of PDEs

$$q_X + 2(W_2^H v_X^2)_X + 2(W_2^H v_X v_Z)_Z = 0, \quad q_Z + 2(W_2^H v_X v_Z)_X + 2(W_2^H v_Z^2)_Z = 0, \quad (4.5a)$$

$$\rho_0 v_{tt} = 2((v_X(W_1^H + W_2^H))_X + (v_Z(W_1^H + W_2^H))_Z), \quad (4.5b)$$

where  $q = p - 2W_1^H - 2(v_X^2 + v_Z^2 + 2)W_2^H$ . Cross differentiating the two equations for  $q$  in (4.5a) yields the compatibility condition

$$((W_2^H v_X v_Z)_X + (W_2^H v_Z^2)_Z)_X - ((W_2^H v_X^2)_X + (W_2^H v_X v_Z)_Z)_Z = 0. \quad (4.6)$$

This condition can be written in the language of vector calculus as

$$\text{curl}(\text{div}(W_2(\|\nabla v\|^2)\nabla v \otimes \nabla v)) = 0.$$

The system (4.5) and (4.6) is overdetermined. Such systems do not typically have solutions, although the problem's nonlinearity makes it difficult to determine existence or uniqueness of solutions with confidence. We also note that, because  $I_1 = u_X^2 + u_Z^2 + 3 = I_2$ , there are many different forms of  $W^H$  resulting in the same equation (4.5b). The strain in a material undergoing a displacement of the form (4.1) is a univariate function of the stress because one can only observe the values of

$$W(I_1) = W^H(I_1, I_1). \quad (4.7)$$

Fitting  $W$  to this material's stress-strain curve provides no information on  $W_1^H$  or  $W_2^H$  individually, but entirely determines the equation (4.5b) as  $W'(I_1) = W_1^H(I_1, I_1) + W_2^H(I_1, I_1)$ . We avoid the intricacies of (4.6) by restricting our attention to generalized neo-Hookean materials, where  $W_2^H = 0$ . This restricts the resulting model's applicability in practice, because there are materials that necessarily depend on  $I_2$ . The issue of determining other conditions on  $W^H$  such that  $W_2^H \neq 0$  and the compatibility condition (4.6) holds for all solutions to (4.5b) has been explored in [21]. This issue is outside the scope of the current work.

Restricting our attention to generalized neo-Hookean materials also makes it easier to determine whether a strain energy density function is polyconvex. In [22, Sec. 2.2], Suchocki *et al.* state that such  $W^H(I_1)$  is polyconvex if and only if  $W^H(I_1)$  is convex. As such, we need only enforce  $W'' > 0$ .

For generalized neo-Hookean materials (i.e.  $W_2^H = 0$ ), the equations for the hydrostatic pressure reduce to,

$$p_X = 2(W'(v_X^2 + v_Z^2))_X, \quad p_Z = 2(W'(v_X^2 + v_Z^2))_Z,$$

yielding the solution in terms of  $v_X$  and  $v_Z$

$$p = 2W'(v_X^2 + v_Z^2) + p_0(t), \quad (4.8)$$

where  $p_0(t)$  is the ambient hydrostatic pressure. If the gravity force  $\mathbf{e} = \rho_0 g \mathbf{e}_Z$  is taken into account, equation (4.8) is replaced by  $p = 2W'(v_X^2 + v_Z^2) + p_0(t) + \rho_0 g Z$ , with  $Z$  directed downward.

**Principal Result 1.** *The  $Y$ -displacement  $v$  of a shear wave given in equation (4.1) travelling through a generalized neo-Hookean material ( $W_2^H = 0$  so  $W = W^H(I_1)$ ) satisfies the nonlinear wave equation (4.5b), explicitly written as*

$$\rho_0 v_{tt} = 2W'(v_X^2 + v_Z^2)(v_{XX} + v_{ZZ}) + 4W''(v_X^2 + v_Z^2)(v_X^2 v_{XX} + 2v_X v_Z v_{XZ} + v_Z^2 v_{ZZ}). \quad (4.9)$$

We refer to equation (4.5b), (4.9) as the *general nonlinear shear wave equation*. The PDE (4.9) is linear if and only if  $W'' \equiv \partial^2 W^H(I_1)/\partial I_1^2 = 0$  (i.e.  $W$  is linear in its single argument  $I_1 - 3$ ). This is the case for Mooney-Rivlin materials with strain energy density function  $W^H = a(I_1 - 3)$ . In this case, the Young's modulus is  $a$ , the wave equation (4.9) reduces to the linear PDE  $\rho_0 v_{tt} = 2a(v_{XX} + v_{ZZ})$ , and the hydrostatic pressure is  $p = 2a + \rho_0 gZ$ .

## 4.2 The general nonlinear shear wave equation for the cubic Yeoh model

Substituting the cubic Yeoh model (3.11) into the general nonlinear shear wave equation (4.9) yields

$$\begin{aligned} \rho_0 v_{tt} = & 2 \left( \mu + M(v_X^2 + v_Z^2) + A(v_X^2 + v_Z^2)^2 \right) (v_{XX} + v_{ZZ}) \\ & + 4 \left( M + 2A(v_X^2 + v_Z^2) \right) (v_X^2 v_{XX} + 2v_X v_Z v_{XZ} + v_Z^2 v_{ZZ}). \end{aligned} \quad (4.10a)$$

The hydrostatic pressure (4.8) in this case is given by

$$p = 2 \left( \mu + M(v_X^2 + v_Z^2) + A(v_X^2 + v_Z^2)^2 \right) + p_0(t) + \rho_0 gZ. \quad (4.10b)$$

Equations (4.10) contain nonlinear polynomial terms of the third and fifth orders in terms of  $v$ . Cubic effects are controlled by the coefficient  $M$  and quintic effects by the coefficient  $A$ .

Writing equation (4.10a) with gradients  $\nabla = \text{grad}_{(X,Z)}$  makes it more apparent what effects each parameter has and that this equation is a total divergence,

$$\frac{\rho_0}{2} v_{tt} = \text{div} \left( \left[ \mu + M \|\nabla v\|^2 + A \|\nabla v\|^4 \right] \nabla v \right). \quad (4.11)$$

The expression in square brackets is  $W_1$  composed with  $\|\nabla v\|^2$ .

To our knowledge, the PDEs (4.10), (4.11) have not previously appeared in the literature. Similar models of nonlinear shear waves based on displacements (4.1) were considered in Kalyanasundaram [23], Teymur [24], and Rushchitsky [25, 26], who assumed a compressible hyperelastic material, and employed a different (Murnaghan) hyperelastic potential. In our approach, because the deformation field (4.1) naturally preserves volumes, new nonlinear wave equations are coupled to the hydrostatic pressure fields that depend on displacements according to (4.10b).

We note that because the nonlinearity in the PDE (4.11) involves only gradients, the dispersion relation for perturbations  $v = v_0 + \epsilon \exp(i(k_1 X_1 + k_3 X_3 - \omega t))$  around a constant equilibrium  $v_0$  coincides with the linear wave equation dispersion relation

$$\omega^2 = \frac{2\mu}{\rho_0} (k_1^2 + k_3^2).$$

However, if the equation (4.11) is linearized about a uniform shear solution  $v = v_0 + sX_1$ ,  $s = \text{const}$ , that is, in the ansatz  $v = v_0 + sX_1 + \epsilon \exp(i(k_1 X_1 + k_3 X_3 - \omega t))$ , the dispersion relation takes the form

$$\omega^2 = \frac{2}{\rho_0} \left( \mu(k_1^2 + k_3^2) + Ms^2(3k_1^2 + k_3^2) + As^4(5k_1^2 + k_3^2) \right).$$

## 5 Nonlinear Viscoelastic shear waves

In this section, we add non-elastic effects responsible for *energy dissipation* to our model. Considering both elasticity and viscosity ensures our model of large displacements in nonlinear materials remain realistic over long periods of time. Materials such as geological formations, composite materials, and biological tissues exhibit viscoelastic properties. Various approaches exist for the mathematical description of viscoelasticity, including rational and irreversible thermodynamics, finite viscoelasticity, and hyper-viscoelasticity. For a more detailed review, see Refs. [9, 14]. In the current work, we use the hyper-viscoelasticity framework [27]. This framework uses both a hyperelastic strain energy density function  $W^H$  to describe elastic effects, and a dissipative potential  $W^V$  to describe viscous phenomena. Hyper-viscoelastic models have also been used in fiber-reinforced material settings [4, 9].

### 5.1 Hyper-viscoelastic constitutive models

In the hyper-viscoelasticity framework, the total stress is represented as a sum of the elastic and the viscous (dissipative) parts

$$W = W^H + W^V. \quad (5.1)$$

$W^V$  is generally a function of  $\mathbf{C}$  and  $\dot{\mathbf{C}} = \partial\mathbf{C}/\partial t$ . For homogenous, isotropic materials,  $W^V$  can be written as a function of up to three independent invariants of  $\mathbf{C}$  and up to seven independent invariants of  $\dot{\mathbf{C}}$ . Invariants of  $\dot{\mathbf{C}}$  are often called pseudo-invariants and similarly,  $W^V$  the pseudo-strain energy density function. The second Piola-Kirchhoff tensor from equation (3.3) is modified as follows to include the viscoelastic stress

$$\mathbf{S}^V = 2\rho_0 \frac{\partial W^V}{\partial \dot{\mathbf{C}}}, \quad (5.2)$$

The total stress tensor is

$$\mathbf{S} = \mathbf{S}^H + \mathbf{S}^V = -p\mathbf{C}^{-1} + 2\rho_0 \left( \frac{\partial W^H}{\partial \mathbf{C}} + \frac{\partial W^V}{\partial \dot{\mathbf{C}}} \right). \quad (5.3)$$

As noted in Section 3, partial derivatives with respect to a matrix/tensor are performed element-wise and symmetrized similar to equation (3.4). The equations of motion of the solid are still given by (3.12), with  $\mathbf{P} = \mathbf{FS}$ .

For the present work, we use the potential given by

$$W^V = \frac{\eta}{4} J_2 (I_1 - 3), \quad J_2 = \text{tr}(\dot{\mathbf{C}}\dot{\mathbf{C}}), \quad (5.4)$$

This convex potential, linear in  $J_2$  and  $I_1 - 3$ , performed well in the short-time memory benchmarks presented by Pioletti et al. [4]. For this benchmark, the authors could accurately fit the single parameter  $\eta$  to the stress-strain curve of several patellar tendons.

To apply the above method, recall the purely elastic model of a shear wave with displacements in the  $Y$ -direction propagating through the  $X-Z$  plane described by (4.1). Viscous effects are added to this setup using the potential  $W^V$  (5.4). The pseudo-invariant  $J_2$  takes the form

$$J_2 = 2(v_{Xt}^2(2v_X^2 + v_Z^2 + 1) + 2v_{Xt}v_{Zt}v_Xv_Z + v_{Zt}^2(v_X^2 + 2v_Z^2 + 1)). \quad (5.5)$$

Using the combined elastic-viscoelastic second Piola-Kirchhoff stress tensor (5.3) to obtain  $\mathbf{P} = \mathbf{FS}$  (cf. (3.3)) and substituting the latter in the general equation of motion (3.12a) with zero forcing (i.e.  $\mathbf{D}_f = \mathbf{0}$ ) yields the following result.

**Principal Result 2.** *The  $Y$ -displacement  $v$  of shear waves (4.1) in the viscoelastic setting with an arbitrary strain energy density function  $W$  and the viscous potential (5.4) satisfies the nonlinear wave equation*

$$\rho_0 v_{tt} = 2((v_X W_1)_X + (v_Z W_1)_Z) + \eta Q[v], \quad (5.6)$$

where  $Q[v]$  is the viscosity term given by

$$\begin{aligned} Q[v] = & (v_X^2 v_{Xt})_X + (v_Z^2 v_{Xt})_X + (v_X^2 v_{Zt})_Z + (v_Z^2 v_{Zt})_Z \\ & + 2(v_X^4 v_{Xt})_X + (v_Z^4 v_{Xt})_X + (v_X^4 v_{Zt})_Z + 2(v_Z^4 v_{Zt})_Z \\ & + ((v_Z^3 v_X + v_X^3 v_Z) v_{Zt})_X + ((v_Z^3 v_X + v_X^3 v_Z) v_{Xt})_Z \\ & + 3(v_Z^2 v_X^2 v_{Xt})_X + 3(v_Z^2 v_X^2 v_{Zt})_Z, \end{aligned} \quad (5.7)$$

Equation (5.6) is the generalization of the nonlinear shear wave equation (4.5b) onto the viscous case, with  $\eta$  denoting a constant viscosity coefficient. By considering only the cubic terms in this equation, one can write  $Q[u]$  as a total divergence,

$$Q[u] \approx \operatorname{div} \left( \|\nabla v\|^2 \nabla v_t \right).$$

The quintic terms can also be written as a divergence of some function applied to  $\nabla v_t$ , but the terms in line 3 of equation (5.7) require swapping the entries of  $\nabla v_t$ . The pressure terms that follow from  $X$ - and  $Z$ -components of the equations of motion yield (cf. (4.5a))

$$p_X = 2(W_1)_X + \eta K_1[v], \quad p_Z = 2(W_1)_Z + \eta K_2[v], \quad (5.8)$$

where  $K_1[v]$ ,  $K_2[v]$  are certain expressions omitted here for brevity. In particular, for the pressure  $p$  to be defined, compatibility conditions  $p_{XZ} = p_{ZX}$  must be satisfied.

In principle, the equation for  $Q[v]$  could be written in terms of an arbitrary viscosity potential; however, the expression is too unwieldy to include here. The given viscosity potential is sufficient for our purposes. Readers wishing to alter our construction by using other viscosity potentials can access our `Maple` script upon request.

## 6 Numerical simulations of hyperelastic and hyper-viscoelastic nonlinear Love wave problems

We now proceed to use the method of lines to numerically study the qualitative behaviour of Love waves propagating through materials governed by the general nonlinear shear wave equations (4.9) and (5.6). First, as a reference, we use the neo-Hookean strain energy density function  $W^H = a(I_1 - 3)$  without viscosity. This results in the familiar linear Love wave equation (2.1). Second, we study a hyperelastic material governed by the cubic Yeoh model described in Subsection 3 without viscosity, resulting in the PDE (4.10a). We finish by studying a hyper-viscoelastic material governed by the cubic Yeoh potential and the viscosity potential from equation (5.4) resulting in the PDE (5.6). In every experiment, we only consider up to cubic terms, neglecting the quintic ones. For Love waves propagating through hyperelastic materials without viscosity, this is equivalent to taking  $A = 0$  in equation (4.10a). After including viscosity, we must additionally assume  $\|\nabla v\|$  is sufficiently small to ensure the quintic terms are dominated by the lower order (linear and cubic) terms.

Similar to Section 2, we model an isotropic layer overlaying an isotropic half-space by considering the coefficient  $\mu$  of  $\Delta v = (v_{xx} + v_{yy})$  to be a piecewise constant function of  $z$ . Every other

parameter is constant across the entire domain. The initial condition is a sudden ‘‘Gaussian explosion’’ centered at a point  $(0, z_0)$ .

$$v(x, z, 0) = A \exp\left(-\frac{x^2 + (z - z_0)^2}{r^2}\right), \quad v_t(x, z, 0) = 0, \quad (6.1)$$

where the explosion’s radius  $r$  is small relative to the size of the domain. We compare the behaviour of each solution when an explosion occurs in the lower half-space ( $z_0 < 0$ ) for  $c_1 < c_2$  and  $c_2 < c_1$ , or the upper layer ( $0 < z_0 < L$ ) for  $c_1 < c_2$ . We do not show the case when the explosion occurs above the interface with  $c_2 < c_1$  because the behaviour is not interesting.

## 6.1 Simulation setup and method for numerical solution

The method of lines transforms the problem of solving a PDE into the problem of solving a system of coupled initial value ODE problems (IVPs), one for each point on the discretized spatial domain. The primary advantage of the method of lines is that there exist fast high-precision methods and their software implementations for numerically solving the resulting IVPs. For the following, we use MATLAB’s `ode23`, which combines Runge–Kutta methods of order 2 and 3 to produce an error estimate after each time step. The method of lines is straightforward to implement for PDEs whose domains simple shapes, such as a rectangle or circle. One alternative to the method of lines is the finite element method provided, for example, by MATLAB’s PDE Toolbox and various other free and proprietary software packages. Finite element methods are better suited for complex domain geometries, but our problem domain is simple. In this setting, the finite element method is largely equivalent to the method of lines but requires more work per time step.

For the PDEs (2.1), (4.10a), and (5.6), we compute an approximate solution over a discretized rectangular domain of width  $W$ , height  $H > L$ , and step size  $h$ . Any point in this discretized domain is of the form

$$(x_j, z_k) = (-W/2 + jh_x, L - kh_z) \\ \in \{-W/2, -W/2 + h_x, \dots, W/2 - h_x, W/2\} \times \{L, L - h_z, \dots, h_z - H, -H\}.$$

One can derive an ODE for a matrix  $U(t)$  such that its  $j, k^{\text{th}}$  entry  $U_{j,k}(t)$  approximates  $v(x_j, z_k, t)$ ; this is achieved using finite differences to approximate spatial derivatives. For example, second-order finite differences yield the ODEs

$$v_{tt}(x_j, z_k, t) \approx c(z_k)^2 \left( \frac{v(x_j + h_x, z_k, t) + v(x_j - h_x, z_k, t) - 2v(x_j, z_k, t)}{h_x^2} + \frac{v(x_j, z_k + h_z, t) + v(x_j, z_k - h_z, t) - 2v(x_j, z_k, t)}{h_z^2} \right)$$

where  $c(z) = c_1$  if  $z$  is in the upper layer (i.e. for  $0 < z < L$ ), and  $c(z) = c_2$  if  $z$  is in the lower half-space (i.e. for  $L < z$ ). The corresponding ODE for the matrix  $U(t)$  is

$$U''_{j,k} = c(z_k)^2 \left( \frac{U_{j+1,k} + U_{j-1,k} - 2U_{j,k}}{h_x^2} + \frac{U_{j,k+1} + U_{j,k-1} - 2U_{j,k}}{h_z^2} \right).$$

This formula is only valid on the interior of the rectangular domain. The remaining points are determined from the boundary conditions. Because the initial condition and each PDE are symmetric about the line  $x = 0$ , we need only compute  $v$  for  $x \geq 0$ .

Our implementation of the method of lines in MATLAB featured second-order finite differences over a rectilinear (nonuniform) mesh. The mesh was chosen such that more grid points

clustered near  $(0, L)$ , and this is for two reasons. First, the displacements  $u$  are largest (and hence the nonlinear effects are most prominent) at the start of the simulation near the source of the explosion  $(0, z_0)$ . As the simulation progresses, the wave travels in all directions with a much smaller amplitude, so it is acceptable to use fewer grid points there. Further, the wave's behaviour above the interface  $z = 0$  where it can interact with both the interface and the surface is of more interest to us than behaviour below the interface. As such, fewer grid points are used below the interface.

To construct this nonuniform partition, we use a pair of smooth monotone functions  $\xi(x), \eta(z) : [0, 1] \rightarrow [0, 1]$  with fixed points at 0 and 1 to transform the uniform discretized domain into a nonuniform one. The nonuniform mesh is then given by  $\xi_j = W\xi(x_j/W + 1/2) - W/2$ ,  $\eta_k = (L + H)\eta((z_k + H)/(L + H)) - H$  and we can solve for the derivatives of  $u$  on the nonuniform mesh with the chain rule. For clarity, let  $v_1$  be the derivative of  $v$  with respect to its first argument. The chain rule applied to  $(v(\xi(x), z))_x$  implies

$$v_1(\xi_j, z) = \frac{(v(\xi_j, z))_1}{\xi'(x_j)}.$$

We may approximate  $(v(W\xi(x_j/W + 1/2) - W/2, z))_1$  with any finite difference method over the uniform partition  $\{x_i\}$  without decreasing that method's rate of convergence, because  $\xi'(x_j)$  is known exactly. For our purposes, the primary advantage of constructing a nonuniform partition in this way is that second order centered finite differences over  $x_{j-1}, x_j, x_{j+1}$  remain second order accurate with the nonuniform mesh. Formulae for  $v$ 's other derivatives follow by the same logic. For both  $\xi$  and  $\eta$ , we use a quadratic of the form  $p(x) = ax^2 + (1 - a)x$  with  $a \in [0, 1]$ . Observe that such  $p$  is monotone increasing with  $p(0) = 0$  and  $p(1) = 1$ . The slope of  $p$  at 0 is  $1 - a$ , and increasing  $a$  causes more mesh points to cluster about 0.

For each of the following simulations, we assume the surface is stress-free, so  $v_z(x, 0, t) = 0$ . To first order, this Neumann boundary condition is equivalent to requiring  $U_{j,0}(t) = U_{j,1}(t)$  for all  $j, t$  (but higher-order approximations would also be reasonable). The other boundaries are modelled as rigid walls (so  $U_{0,k} = U_{\text{end},k} = U_{j,\text{end}} = 0$  for all  $j, k$ ), but  $W, H$  are sufficiently large such that these boundary conditions are irrelevant to the simulation. We solve the resulting system of ODEs in MATLAB with the function `ode23`. This function is chosen because it (1) somewhat accounts for the stiffness inherent in equations with damping such as parabolic equations when discretized by the method of lines, (2) does not evaluate the ODE's Jacobian, and (3) uses vector-level parallelism to compute the 3D solution matrix  $U$  with repeated matrix addition and scalar multiplication. The linear wave equation and inviscid equation (4.10a) are likely not stiff because they do not possess any damping terms. The equation (5.6) likely is stiff 1. because of the damping and 2. nonstiff solvers struggle to solve the equation numerically. MATLAB has various stiff ODE solvers such as `ode15s` or `ode23s`, but these require evaluating the ODE's Jacobian. The Jacobian of our ODE is very large because we took the mesh as fine as reasonably possible on our machine. For each simulation, there were about  $250^2$  mesh points resulting in  $2 \times 250^2$  ODEs (one ODE for  $v$  and another for  $v_t$  for each mesh point). Each ODE depends on the the 4 points neighbouring  $(x_j, z_k)$ . As such, the Jacobian would be a (sparse) matrix of size  $2 \times 250^2 \times 250^2 \approx 10^{10}$  and contain at least  $2 \times 4 \times 250^2 \approx 10^5$  nonzero entries. Further, the nonlinearity of this PDE system makes the Jacobian's entries nonconstant and tricky to quickly compute for each time step. As such, we believe the stiff solvers are likely not worth the effort and increased memory usage over `ode23`.

## 6.2 Linear shear waves and linear Love waves

Figures 6.1, 6.3, and 6.5 contain colour plots of a solution of the linear Love wave equation (2.1) for various times and values of  $z_0, c_1$ , and  $c_2$ . The initial condition is in the top left corner

of each figure, and the interface in each plot is marked by a change of opacity. We can tell which domain has the faster wave speed based on how distorted the wave’s curvature is. If  $c_1 < c_2$  then the outermost wave propagating below the interface looks qualitatively more like a semi-circle than if  $c_2 < c_1$ . Whenever a wave crosses the interface, a reflection/refraction interaction occurs. So, some proportion of the wave crossing the interface will reflect and travel in the opposite direction instead of continually travelling in a straight line. Because the surface is free of damping, the entire wave is reflected at the surface of the domain. In particular, it is of interest to observe the case when  $c_2 < c_1$  (Figure 6.5), which violates the Love wave existence condition (2.6). In the numerical solution, unlike the cases when  $c_1 < c_2$  (e.g., Figure 6.1), most of the wave energy remains below the interface, while the wave above the interface appears to decay in time.

Figures 6.2, 6.4, and 6.6 plot the speed of the wave’s propagation along the interface and the surface of the simulations from figures 6.1, 6.3, and 6.5 respectively. Recall the linear Love wave existence condition (2.5) which requires these wave speeds be between  $c_1$  and  $c_2$ . In every simulation we performed, the wave propagating along the interface always tended to the maximum of  $\{c_1, c_2\}$ . For the surface, the waves eventually tended to the maximum of  $\{c_1, c_2\}$ . We see in Figure 6.4 that the wave speed along the surface is only *initially* near the minimum of  $\{c_1, c_2\}$  when  $c_1 < c_2$  and the explosion originates from the upper layer. The wave speed eventually tends to the larger wave speed because a faster moving wave reflected from the surface becomes the outermost wave. Some time must pass until the wave travels to the surface and to the interface, and until then, the surface and interface velocities may be taken to be zero. Changing of initial  $z$ -position and the spike width for the initial explosion further from the interface results in corresponding different time of surface/interface wave emergence. Because our interest lies mostly in studying the wave’s interactions with the interface, we save computational resources by making the explosion close to the interface.

In Section 2, we derived a family of solutions to the linear Love wave equation by assuming the phase of each individual mode is constant with respect to  $z$ . This assumption does not agree with the results derived from figures 6.2 and 6.4; however, it becomes more reasonable as the simulations continue. Indeed, the set of solutions derived in Section 2 does not correspond to the initial conditions we simulated.

To compute the wave speed along the surface (and the interface after making minor changes to the following), we first find the largest value of  $x_s$  such that  $|u(x_s, L, t_s)|$  is greater than some numerical epsilon (in our case,  $10^{-3}$ ) for each nonuniform time step of the simulation  $t_s$ . The velocity is then approximated with first-order forward differences

$$v_s \approx \frac{x_s - x_{s-1}}{t_s - t_{s-1}}.$$

Rather than use the data  $U_{,0}(t_s) \approx u(x, L, t_s)$  directly, we build a spline from  $U_{,0}(t_s)$  and evaluate the spline on 500 times more points. Using a spline is important because  $x_{s+1}$  might not change over the time  $[t_s, t_{s+1}]$  if the mesh is not sufficiently fine or the time step is too small. In each of our simulations, we already take the step size  $h$  as small as we can before our server runs out of RAM (128GB) and resorts to swap instead. As such, the spline roughly increases the resolution of the data specifically along the surface.

We must ensure the adaptive time step  $\Delta t_s = t_{s+1} - t_s$  is not too small when computing  $v_s$ , because subtraction, and hence finite differences, are not well conditioned. So, before plotting the wave speeds, we cull several time steps so that the resulting  $\Delta t_s$  is greater than some numerical epsilon (in our case,  $\Delta t_s > 10^{-3}$ ). Culling is especially important in subsections 6.3 and 6.4 because the ODEs resulting from discretizing the PDEs (4.9) and (5.6) are especially stiff during the initial explosion. For our choice of parameters, such stiffness causes `ode23` to

take such small time steps that over 90% of the time steps are culled. We use this algorithm on  $|u(x_s, 0, t_s)|$  to compute the wave speed along the interface as well. This culling is exclusively for computing and plotting the wave velocity.

### 6.3 Nonlinear shear and Love-type waves

Now, we study the qualitative behaviour of the numerical solutions of equation (4.10a) (resulting from the cubic Yeoh strain energy density function (4.9)) applied to Love waves propagating through hyperelastic materials,

$$\frac{\rho_0}{2}v_{tt} = \operatorname{div} \left( [\mu(z) + M\|\nabla v\|^2 + A\|\nabla v\|^4] \nabla v \right). \quad (6.2)$$

In each experiment, we take  $A = 0$ , ignoring the quintic terms. Again, we model an isotropic layer overlying an isotropic elastic half-space by taking  $\mu(z)$  to be a step function.

Figures 6.7, 6.9, and 6.11 show the similar plots to those of the previous subsection, but for the numerical solution of (6.2) with  $M = 5 \cdot 10^{-5}$ . The solution's qualitative behaviour is very similar to that of the linear case, even though  $M$  was taken as large as possible within the constraints of system memory. Increasing  $M$  appears to result in a higher frequency of small oscillations in the plots of  $v(x, z, t)$ . It is easier to see these small oscillations after the explosion splits in all directions, greatly decreasing the amplitude. In the plots of the wave speeds (Figures 6.8, 6.10, and 6.12) we observe similar qualitative behaviour as in the linear case shown above. In particular, there exists an initial period of time where the velocity at the surface is zero; the wave speed along the surface is only initially the minimum of  $\{c_1, c_2\}$  when  $c_1 < c_2$  and the explosion originates from the upper layer; the velocities at the surface and interface eventually agree by tending to the value of the maximum of  $\{c_1, c_2\}$ .

### 6.4 Hyper-viscoelastic shear and Love-type waves

We now study the qualitative behaviour of the numerical solutions of equation (5.6) (resulting from the cubic Yeoh strain energy density function (4.9) and the viscosity potential (5.4)) applied to Love waves propagating through hyper-viscoelastic materials. In each experiment, we take  $A = 0$  and ignore any quintic effects in the dispersion term  $Q[v]$ . The resulting model is

$$\begin{aligned} \rho v_{tt} = & 2\mu(v_{xx} + v_{zz}) \\ & + 2M \left( (v_x^2 + v_z^2)(v_{xx} + v_{zz}) + 2(v_x^2 v_{xx} + v_z^2 v_{zz} + 2v_x v_z v_{xz}) \right) \\ & + \eta \left( (v_x^2 + v_z^2)(v_{xxt} + v_{zzt}) + 2v_{xt}(v_x v_{xx} + v_z v_{xz}) + 2v_{zt}(v_x v_{xz} + v_z v_{zz}) \right). \end{aligned} \quad (6.3)$$

Figures 6.13, 6.15, and 6.17 show surface plots of a numerical solution  $v(x, z, t)$  of equation (6.3) with  $M = 5 \cdot 10^{-5}$  and  $\eta = 3.5 \cdot 10^{-4}$ . The behaviour is again similar to that described in the above two subsections; however, the waves disperse much more rapidly throughout the domain. When  $c_1 < c_2$ , the maximum value of  $u(x, z, 7.5)$  (the point of largest displacement at the end of the simulation) is much less than the equivalent simulation in the previous sections (likely due to the dissipation of energy). When  $c_2 < c_1$  and the Gaussian explosion occurs below the interface (Figure 6.17), the displacement  $v(x, z, t) < 0$  for more values of  $x, z$  than any of the other experiments. Our plots of the wave speeds 6.14, 6.16, and 6.18 again shows similar behaviour to the prior two subsections.

Figure 6.19 plots envelopes of the solution  $v(x, 0, t)$  and  $v(x, L, t)$  of equation (6.3) for four values of  $t$  and four values of  $\eta$ . We see the waves behave much more predictably as  $\eta$  increases. For smaller  $\eta$ , the waves travelling at the surface appear to skew to the right. In the sequel, we study the 1D version of equation (6.3). In this 1D setting,  $v_{xt}(x, t)$  is unbounded when  $x$  is a local maximum of  $v(x, t)$ . This is not what we observe in the 2D case.

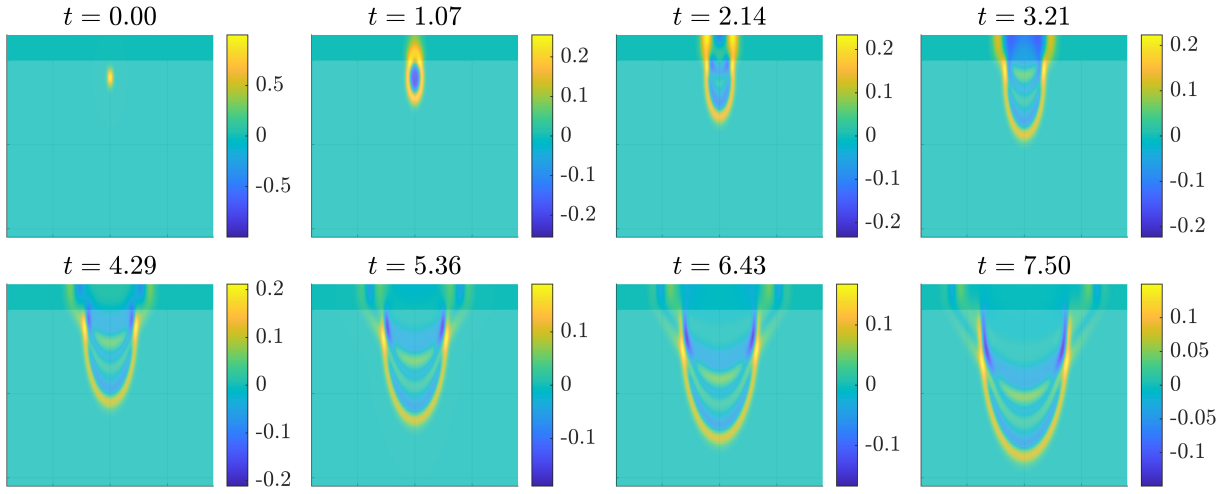


**Figure 6.1:** Plots of a numerical solution  $u(x, z, t)$  of equation (2.1) with  $c_1 < c_2$  after a Gaussian explosion centered in the lower half-space (i.e.  $z_0 < 0$  in equation (6.1)). In this and any similar surface plots in this section,  $x$  changes over the horizontal axis and  $z$  changes over the vertical axis. The parameters are  $c_1 = 0.1$ ,  $c_2 = 0.2$ ,  $z_0 = -0.1$ ,  $r = 0.05$ ,  $A = 1$ ,  $L = 0.15$ ,  $W = 3.6$ ,  $H = 1.8$ , and  $h = 0.005$ .

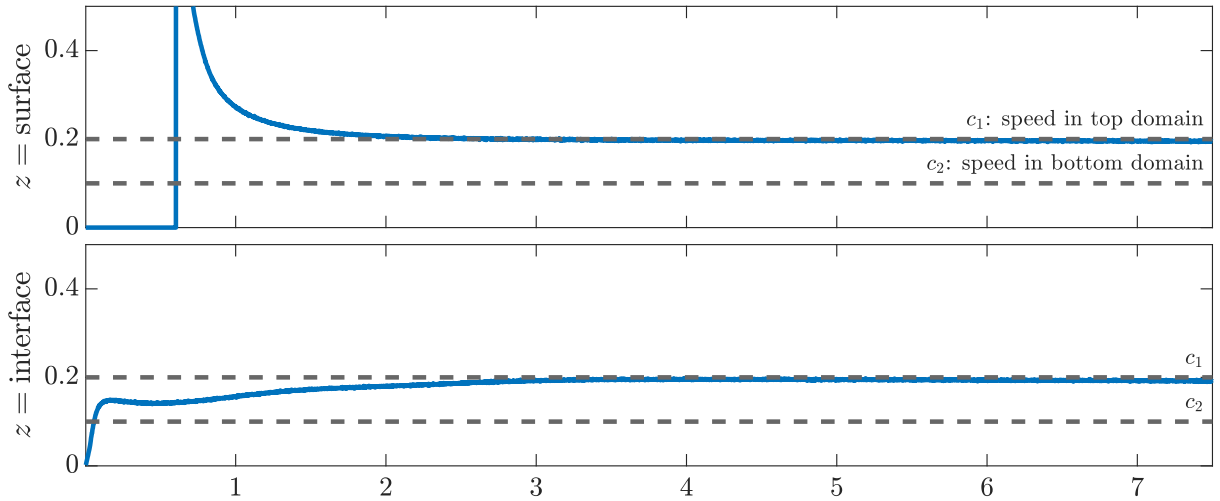


**Figure 6.2:** Speed of propagation along the interface and surface of Figure 6.1 over time.

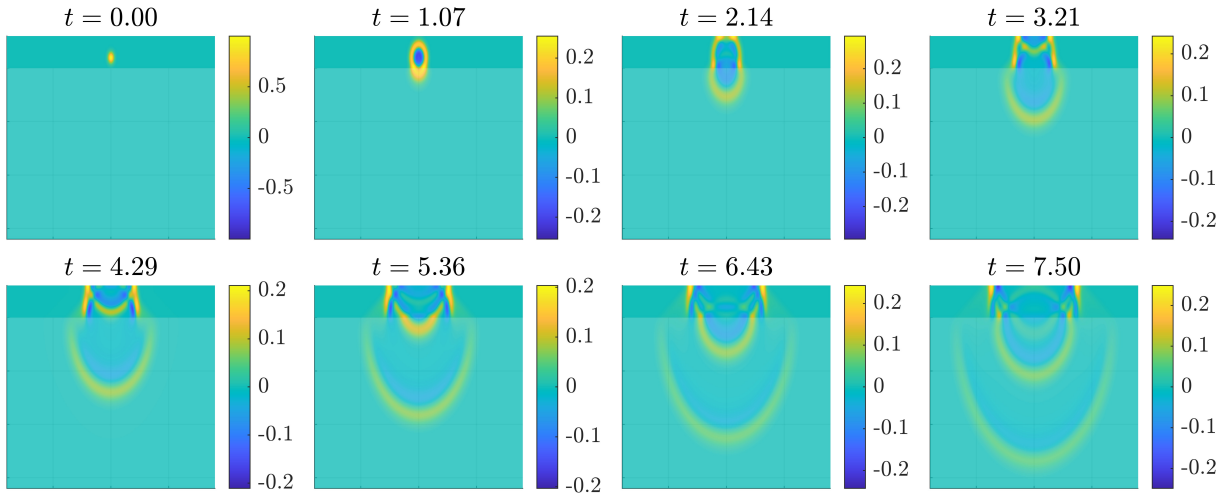


**Figure 6.3:** Plots of a numerical solution of (2.1) with  $c_1 < c_2$  and  $z_0$  in the upper layer. The parameters (bolded to emphasize parameters that differ from previous figures) are  $c_1 = 0.1$ ,  $c_2 = 0.2$ ,  $z_0 = \mathbf{0.1}$ ,  $r = 0.05$ ,  $A = 1$ ,  $L = \mathbf{0.3}$ ,  $W = 3.6$ ,  $H = \mathbf{1.6}$ , and  $h = 0.005$ .

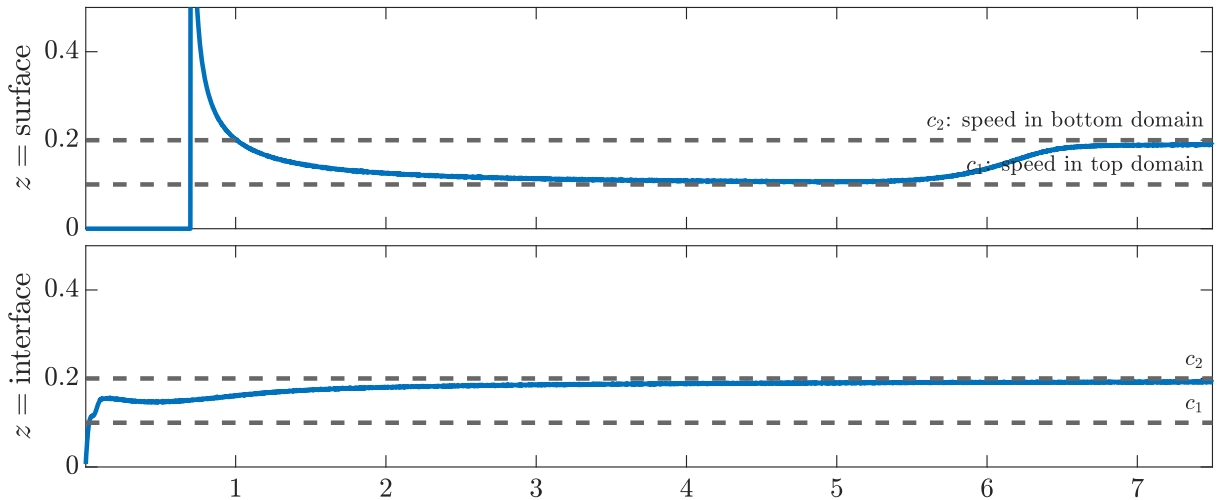


**Figure 6.4:** Speed of propagation along the interface and surface of Figure 6.3 over time. The outermost wave at the interface suddenly moves at speed  $c_2$  around  $t = 6.5$  because that is when a faster moving wave is reflected from the surface of the domain passes the initial wave.

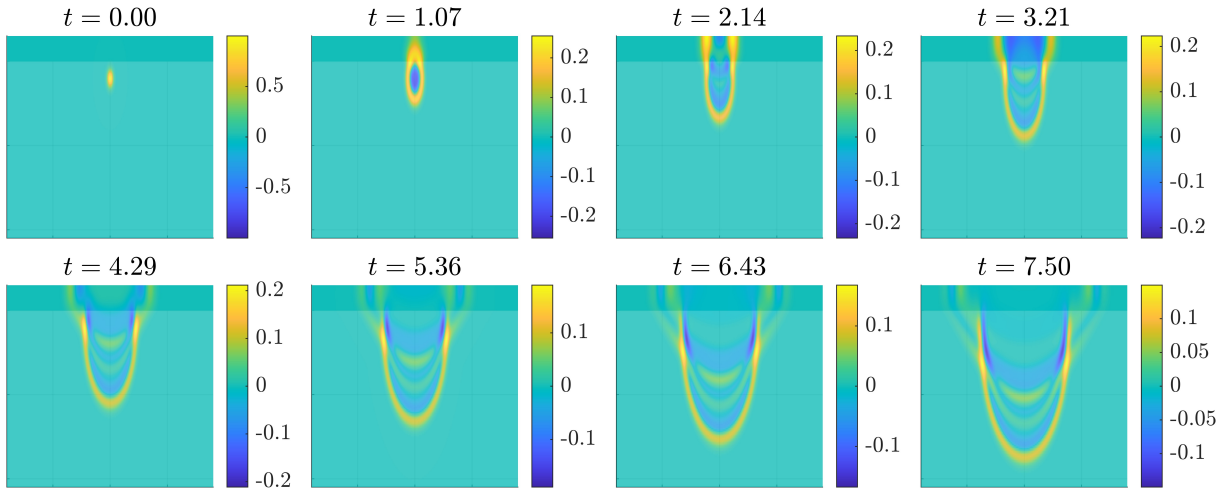


**Figure 6.5:** Plots of a numerical solution of (2.1) with  $c_1 > c_2$  and  $z_0$  in the lower half-space. The parameters are  $c_1 = 0.2$ ,  $c_2 = 0.1$ ,  $z_0 = -0.1$ ,  $r = 0.05$ ,  $A = 1$ ,  $L = 0.15$ ,  $W = 3.6$ ,  $H = 1.05$ , and  $h = 0.005$ .

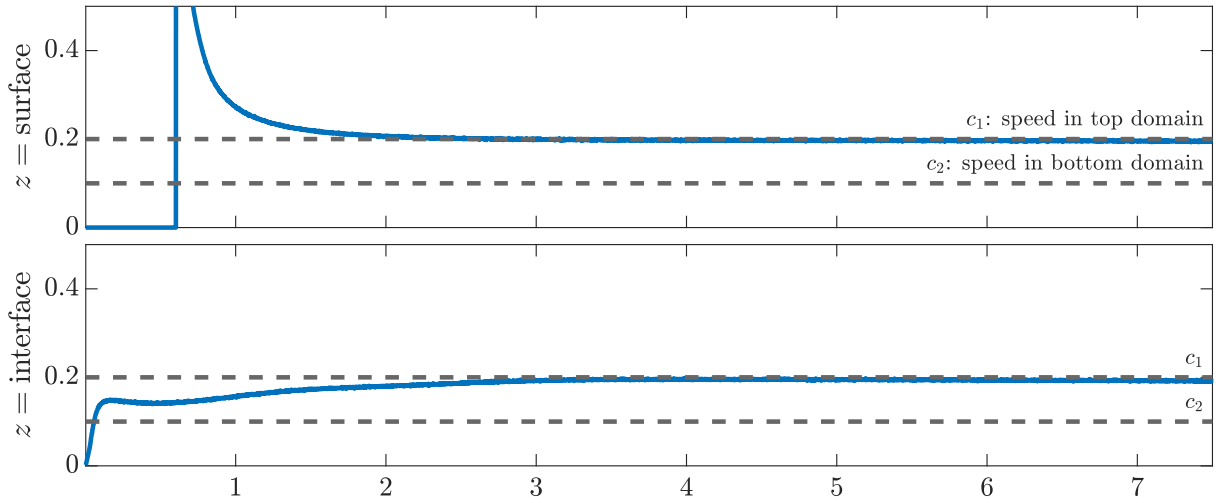


**Figure 6.6:** Speed of propagation along the interface and surface of Figure 6.5 over time.

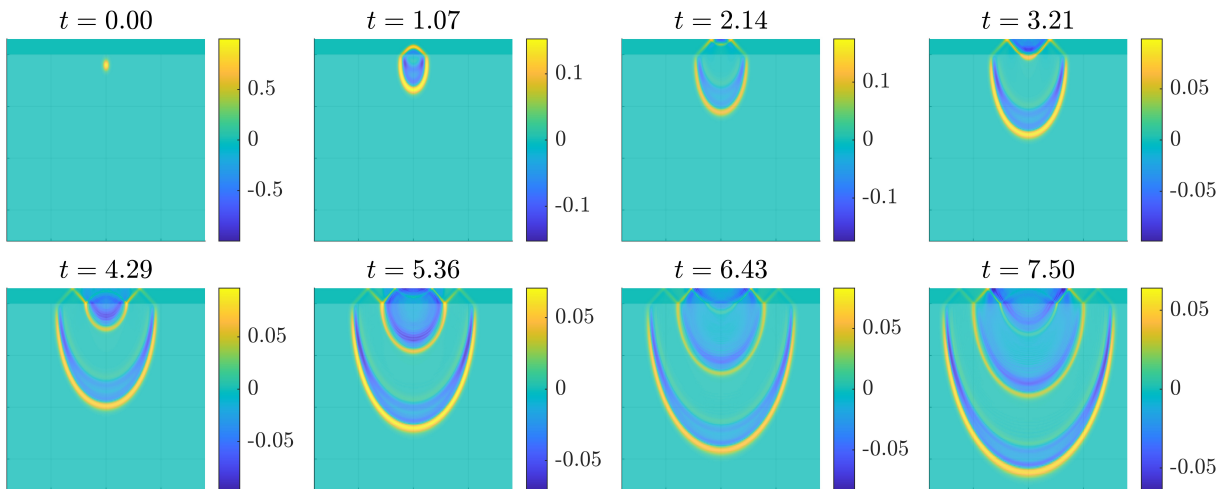


**Figure 6.7:** Plots of a numerical solution of (6.2) with  $c_1 < c_2$  and  $z_0$  in the lower half-space. The parameters are  $c_1 = 0.1$ ,  $c_2 = 0.2$ ,  $z_0 = -0.1$ ,  $r = 0.05$ ,  $A = 1$ ,  $L = 0.15$ ,  $M = 5 \cdot 10^{-5}$ ,  $W = 3.6$ ,  $H = 1.8$ , and  $h = 0.0068$ .

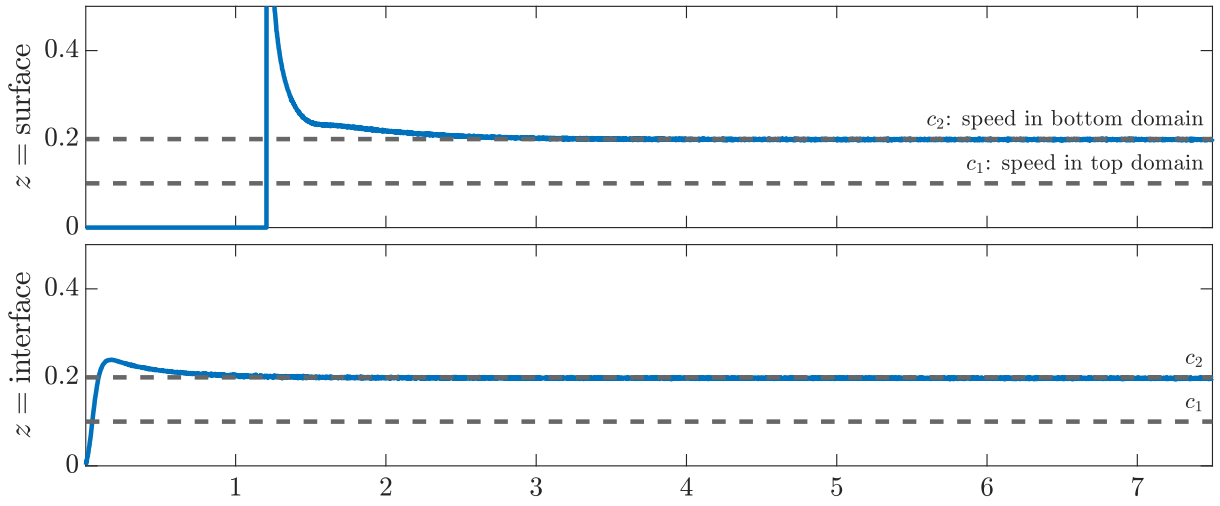


**Figure 6.8:** Speed of propagation along the interface and surface of Figure 6.7 over time.

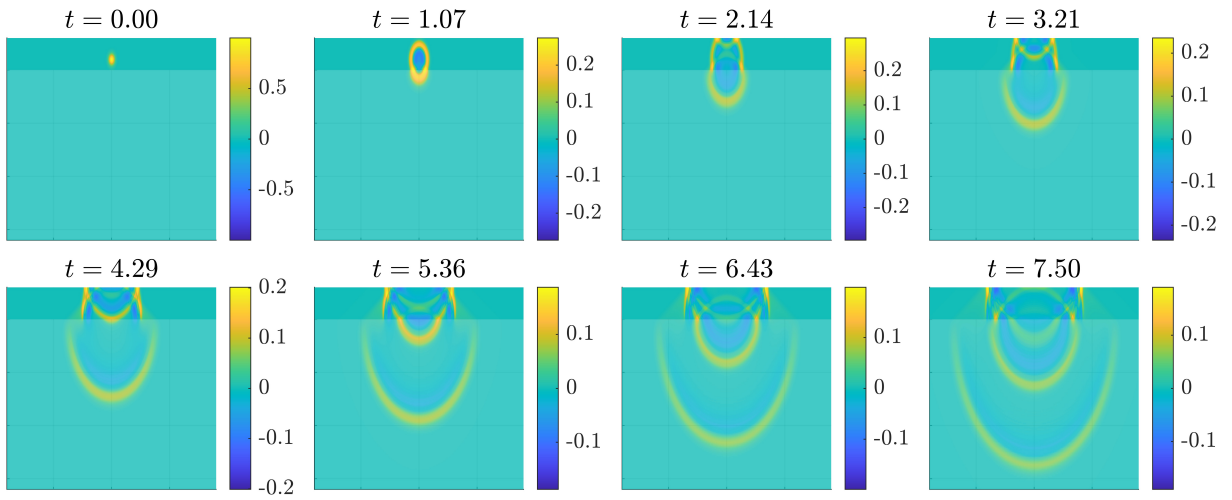


**Figure 6.9:** Plots of a numerical solution of (6.2) with  $c_1 < c_2$  and  $z_0$  in the upper layer. The parameters are  $c_1 = 0.1$ ,  $c_2 = 0.2$ ,  $z_0 = 0.1$ ,  $r = 0.05$ ,  $A = 1$ ,  $L = 0.3$ ,  $M = 5 \cdot 10^{-5}$ ,  $W = 3.6$ ,  $H = 1.6$ , and  $h = 0.0068$ .

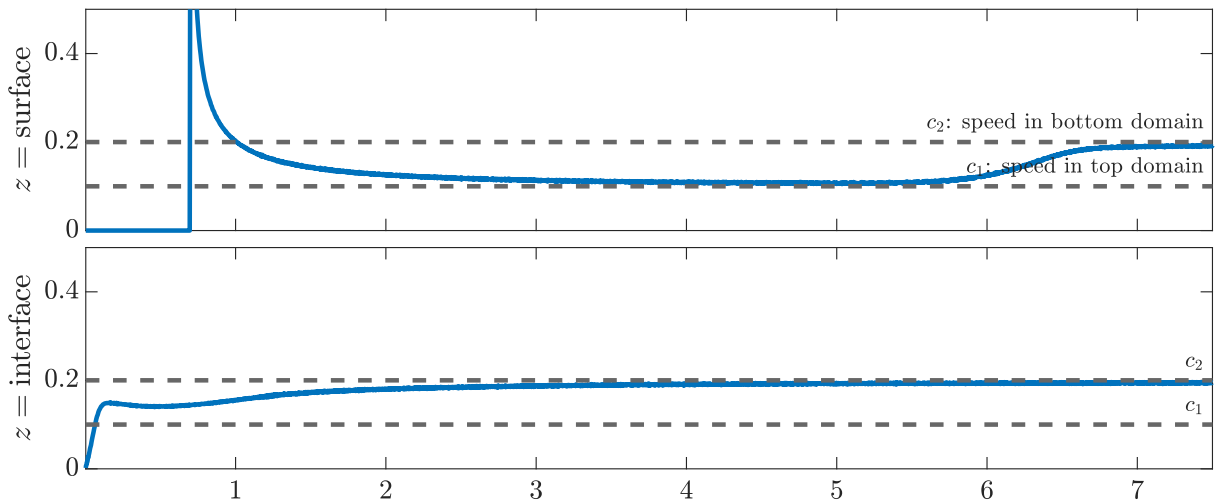


**Figure 6.10:** Speed of propagation along the interface and surface of Figure 6.9.

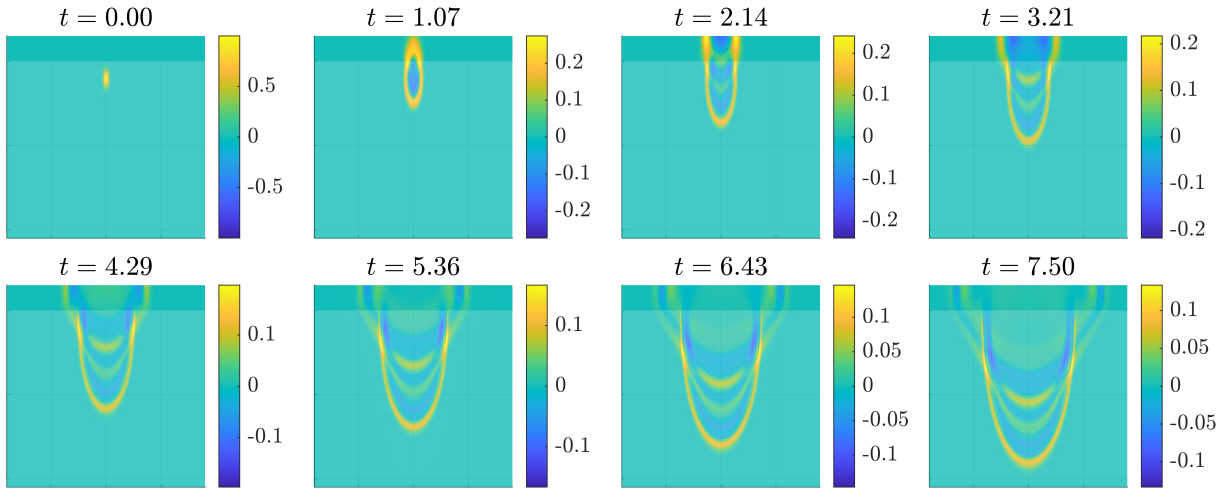


**Figure 6.11:** Plots of a numerical solution of (6.2) with  $c_1 > c_2$  and  $z_0$  in the lower half-space. The parameters are  $c_1 = 0.2$ ,  $c_2 = 0.1$ ,  $z_0 = -0.1$ ,  $r = 0.05$ ,  $A = 1$ ,  $L = 0.15$ ,  $M = 5 \cdot 10^{-5}$ ,  $W = 3.6$ ,  $H = 1.05$ , and  $h = 0.0068$ .

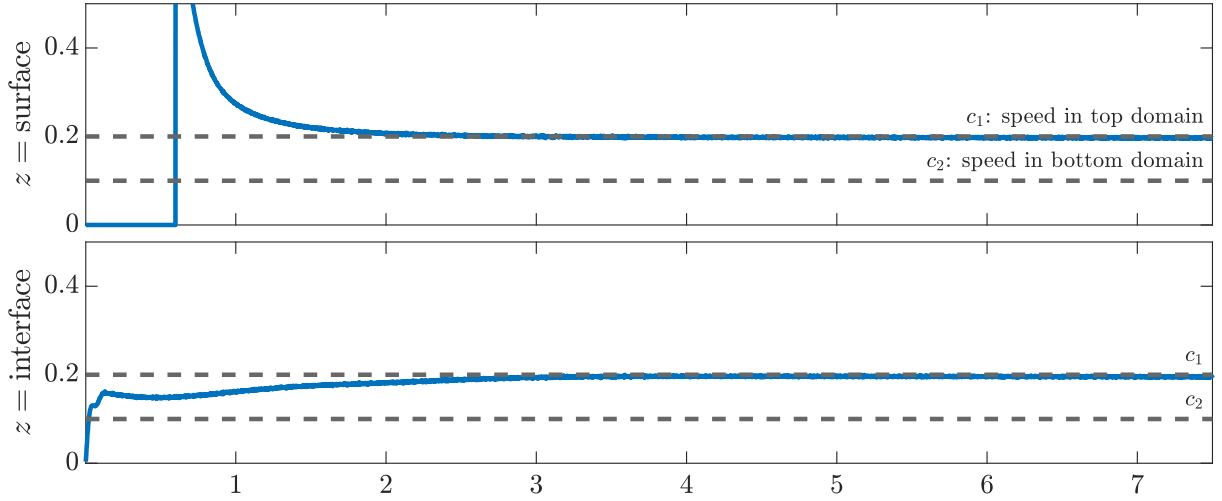


**Figure 6.12:** Speed of propagation along the interface and surface of Figure 6.11 over time.

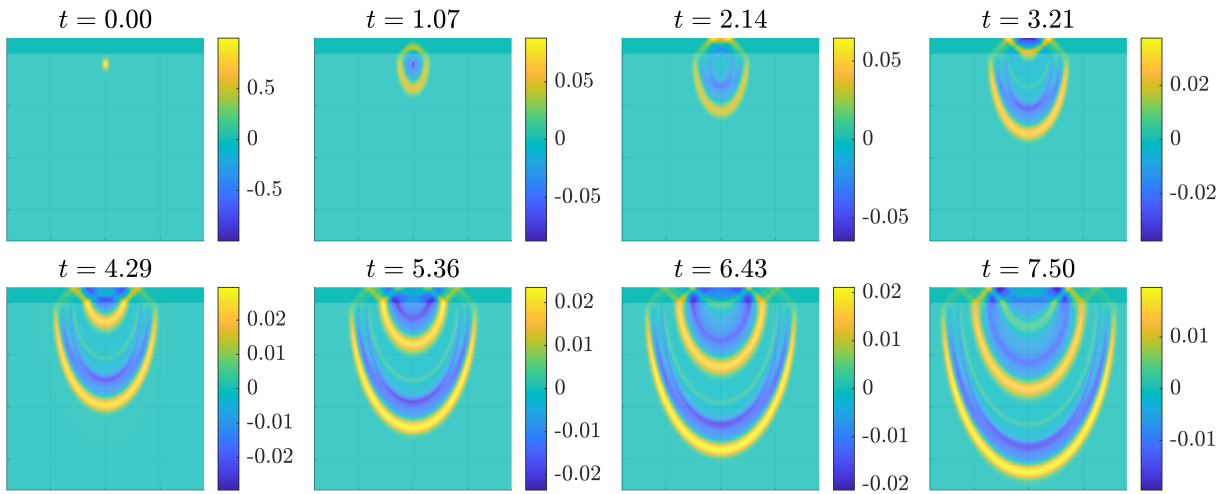


**Figure 6.13:** Plots of a numerical solution of (6.3) with  $z_0$  in the lower half-space. The parameters are  $c_1 = 0.1$ ,  $c_2 = 0.2$ ,  $z_0 = -0.1$ ,  $r = 0.05$ ,  $A = 1$ ,  $L = 0.15$ ,  $M = 5 \cdot 10^{-5}$ ,  $\eta = 3.5 \cdot 10^{-4}$ ,  $W = 3.6$ ,  $H = 1.8$ , and  $h = 0.0068$ .

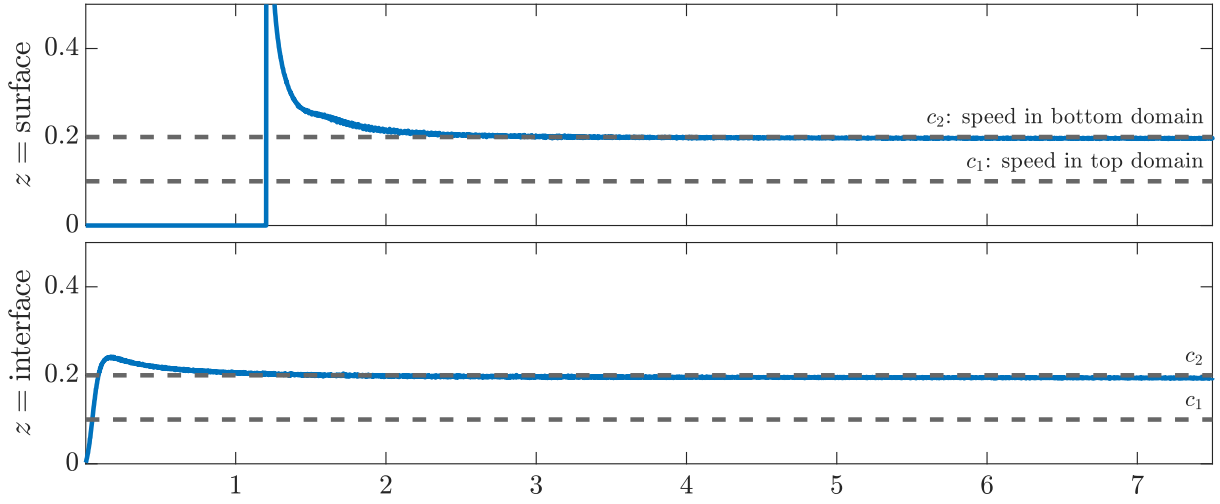


**Figure 6.14:** Speed of propagation along the interface and surface of Figure 6.13.

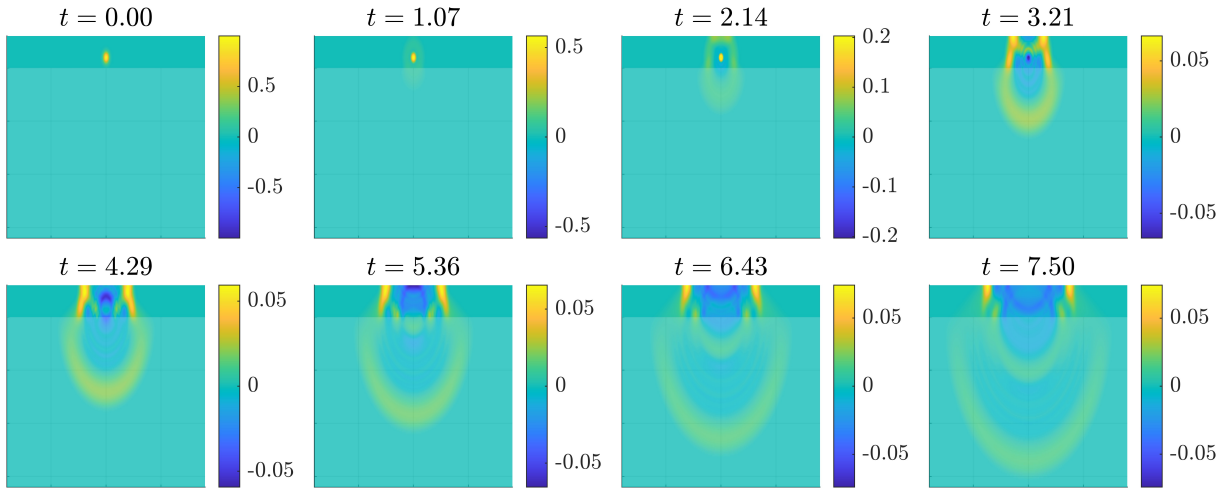


**Figure 6.15:** Plots of a numerical solution of (6.3) after a Gaussian explosion centered in the upper layer. The parameters are  $c_1 = 0.1$ ,  $c_2 = 0.2$ ,  $z_0 = 0.1$ ,  $r = 0.05$ ,  $A = 1$ ,  $L = 0.3$ ,  $M = 5 \cdot 10^{-5}$ ,  $\eta = 3.5 \cdot 10^{-4}$ ,  $W = 3.6$ ,  $H = 1.05$ , and  $h = 0.0068$ .

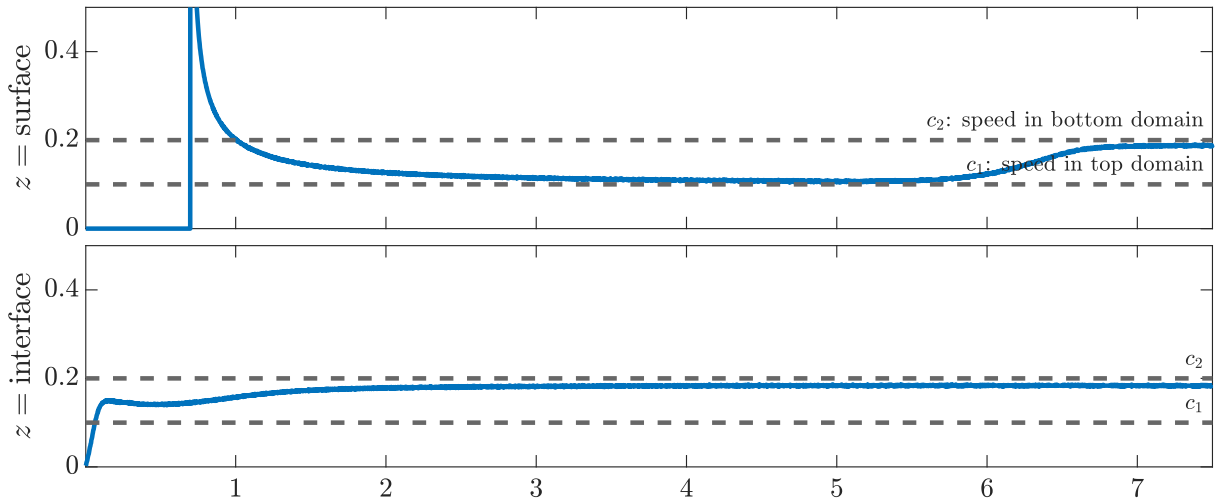


**Figure 6.16:** Speed of propagation along the interface and surface of Figure 6.15.

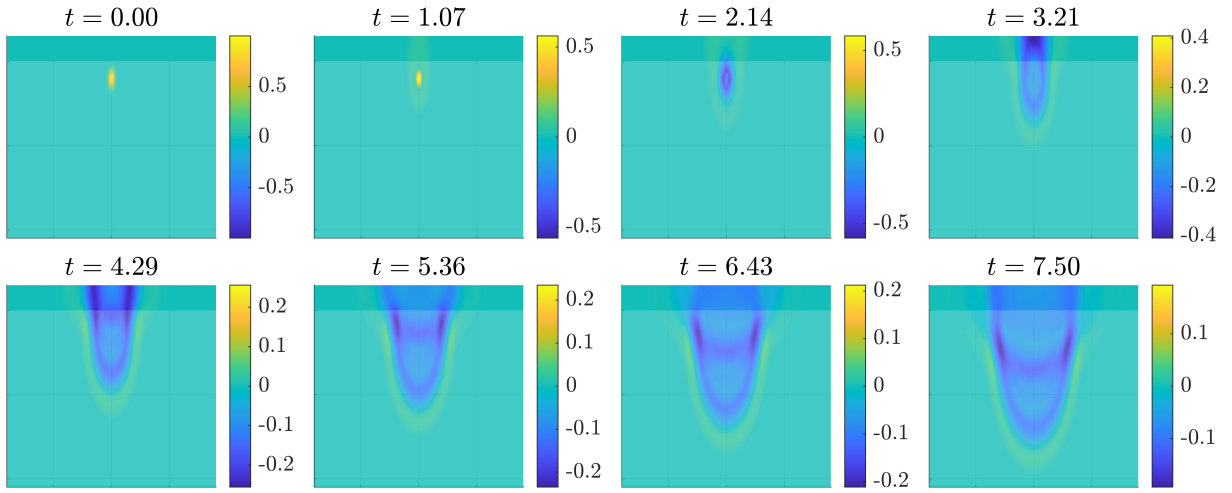


**Figure 6.17:** Plots of a numerical solution of (6.3) with  $c_1 > c_2$  after a Gaussian explosion centered in the lower half-space. The parameters are  $c_1 = 0.2$ ,  $c_2 = 0.1$ ,  $z_0 = -0.1$ ,  $r = 0.05$ ,  $A = 1$ ,  $L = 0.15$ ,  $M = 5 \cdot 10^{-5}$ ,  $\eta = 3.5 \cdot 10^{-4}$ ,  $W = 3.6$ ,  $H = 1.05$ , and  $h = 0.0068$ .

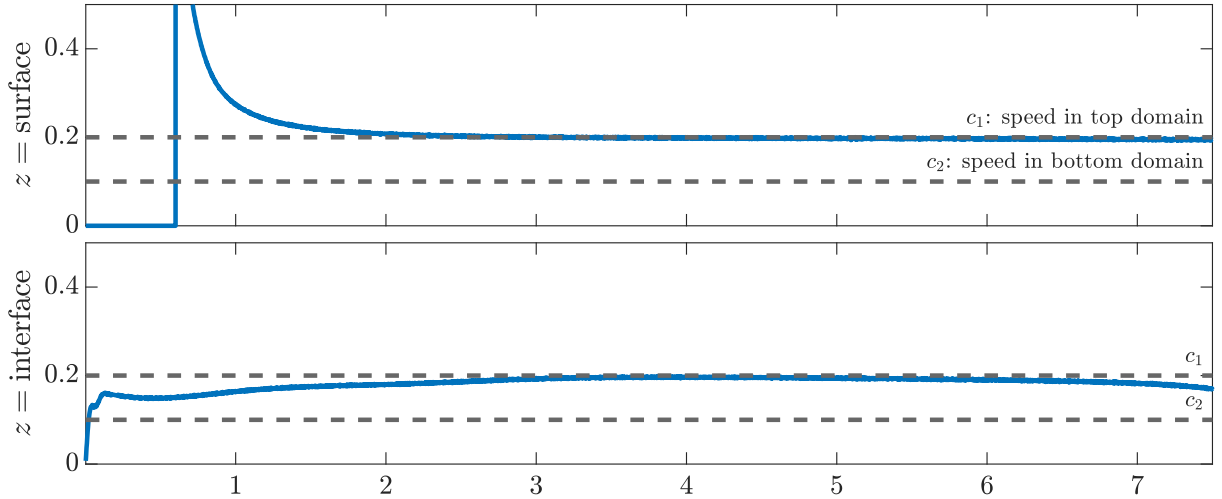


**Figure 6.18:** Speed of propagation along the interface and surface of Figure 6.17.

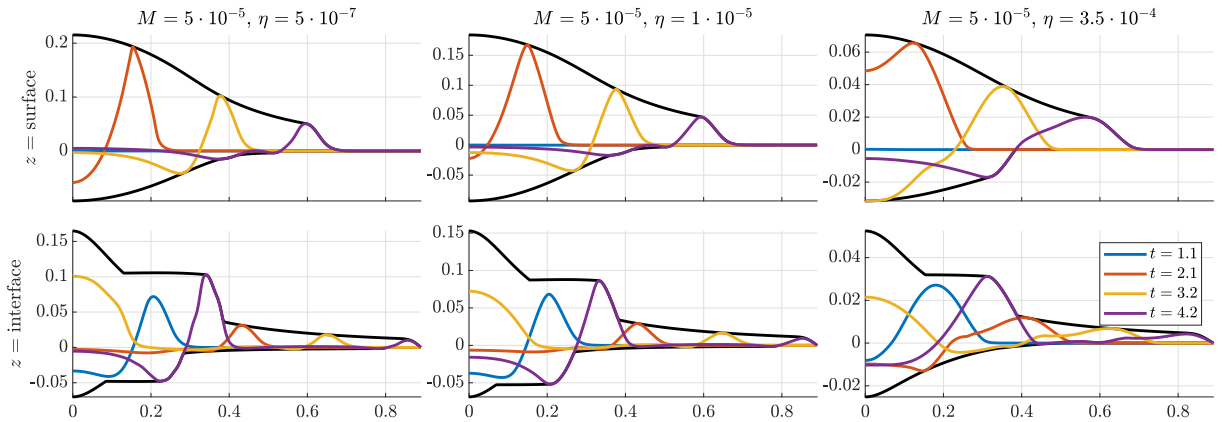


**Figure 6.19:** Plots of numerical solutions  $v(x, z, t)$  of (6.3) over  $x$  (horizontal axis) for fixed  $z$  along the interface and top of the domain with  $c_1 < c_2$  after a Gaussian explosion in the lower half-space for various values of  $\eta$ . The parameters are  $c_1 = 0.1$ ,  $c_2 = 0.2$ ,  $z_0 = -0.1$ ,  $r = 1/16$ ,  $A = 0.3$ ,  $L = 0.15$ ,  $W = 2.1$ ,  $H = 2.45$ , and  $h = 0.068$ .

## 7 Symmetry analysis of the one-dimensional model

We are interested in applying the Lie symmetry method to the 1D version of equation (6.3), given by

$$\rho u_{tt} = 2(\mu + 3Mu_x^2)u_{xx} + \eta(u_{xt}u_x^2)_x. \quad (7.1)$$

The Lie symmetries of a PDE, when they exist, are of interest because they provide an algorithmic way of deriving special sets of exact solutions, namely, invariant solutions. They are one of few methods for deriving solutions to nonlinear PDEs. Further, many familiar ansätze (such as the travelling wave ansatz or the self-similar ansatz) are special cases of Lie symmetries.

Equation (7.1) can be nondimensionalized by dividing both sides by  $\rho \neq 0$  and setting

$$t = \frac{\eta}{6M}T, \quad x = \frac{\eta}{M}\sqrt{\frac{\mu}{18}}X, \quad u(x, t) = \frac{\eta\mu}{\sqrt{54M^3}}U(X, T).$$

The resulting equation becomes

$$U_{TT} = (1 + U_X^2)U_{XX} + (U_{XT}U_X^2)_X = U_{XX} + U_X^2U_{XX} + (U_X^2U_{XX})_T. \quad (7.2)$$

It is straightforward to use a computer algebra software package to compute each point symmetry of (7.2). The four symmetry generators of (7.2) as computed via the implementation of Lie's algorithm in the Maple package GeM [28, 29] are

$$X_1 = \frac{\partial}{\partial x}, \quad X_2 = \frac{\partial}{\partial t}, \quad X_3 = \frac{\partial}{\partial u}, \quad X_4 = t\frac{\partial}{\partial u}.$$

Because Lie's algorithm is complete, these four generators form a basis of the Lie algebra of point symmetries of (7.2). Several families of solutions to equation (7.2) can be derived by studying the invariant curves of a linear combination of these symmetry generators. The first integrals of

$$X = c\frac{\partial}{\partial x} + \frac{\partial}{\partial t} + (k_1 + tk_2)\frac{\partial}{\partial u}, \quad (7.3)$$

for constants  $c, k_1, k_2 \in \mathbb{C}$  are  $I_1 = x - ct$  and  $I_2 = k_1t + k_2t^2/2 - u$ , so one family of solutions is of the form  $u(x, t) = k_1t + k_2t^2/2 + F(x - ct)$ , where  $F$  is any solution to the ODE

$$cF'^2F''' = F''(F'^2 - 2cF'F'' + 1 - c^2) - k_2. \quad (7.4)$$

If we require  $u(x, t)$  to be bounded over  $t$ , then  $k_1 = k_2 = 0$  and equation (7.4) simply describes the travelling wave solutions of the PDE (7.2). It is straightforward to derive an exact solution when  $c = \pm 1$ . In this case, the ODE becomes  $F'''/F'' + 2F''/F' = \pm 1$ , which yields the family of exact solutions

$$F(x) = c_1 + \int_0^x \sqrt[3]{c_2 e^{\text{sign}(c)w} + c_3} dw \quad (7.5)$$

for some real constants  $c_1, c_2, c_3$ . A physically realizable wave-type travelling wave solution must be bounded and possess a local extremum. No choice of  $c_1, c_2, c_3$  leads to a bounded solution over all of  $\mathbb{R}$ ; however, one endpoint ( $\pm\infty$ ) can be bounded by taking  $c_3 = 0$ . A critical point  $x_c$  of  $F$  only exists when  $c_2$  and  $c_3$  have different signs. Such  $x_c$  is a local maximum or minimum because  $F''(x_c) = \pm\infty$ . Figure 7.1 plots such a solution  $F$ . For comparison, Figure 7.2 uses the method of lines to plot a numerical solution of (7.2) for various times after a Gaussian explosion.

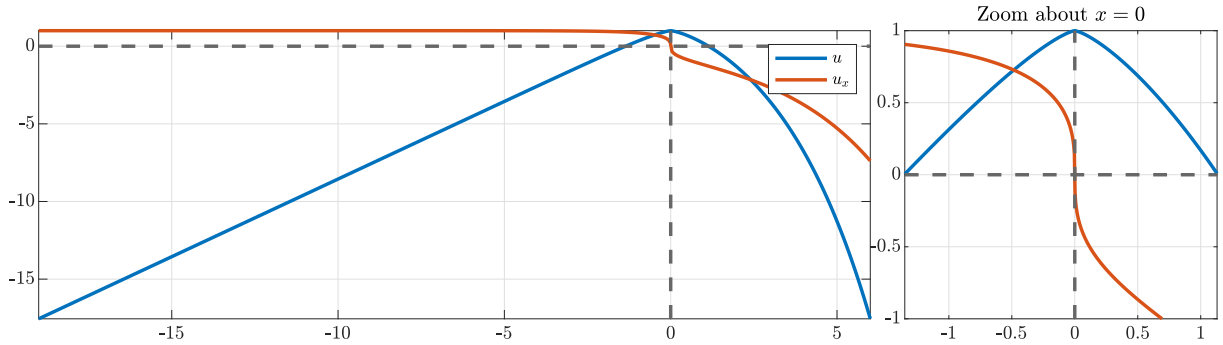


**Figure 7.1:** Solution (7.5) and its spatial derivative using  $c_1 = 1$ ,  $c_2 = -1$ , and  $c_3 = -c_2$ . When comparing this to other plots, note that for the travelling wave with  $c = 1$ ,  $u_x = -u_t$ .

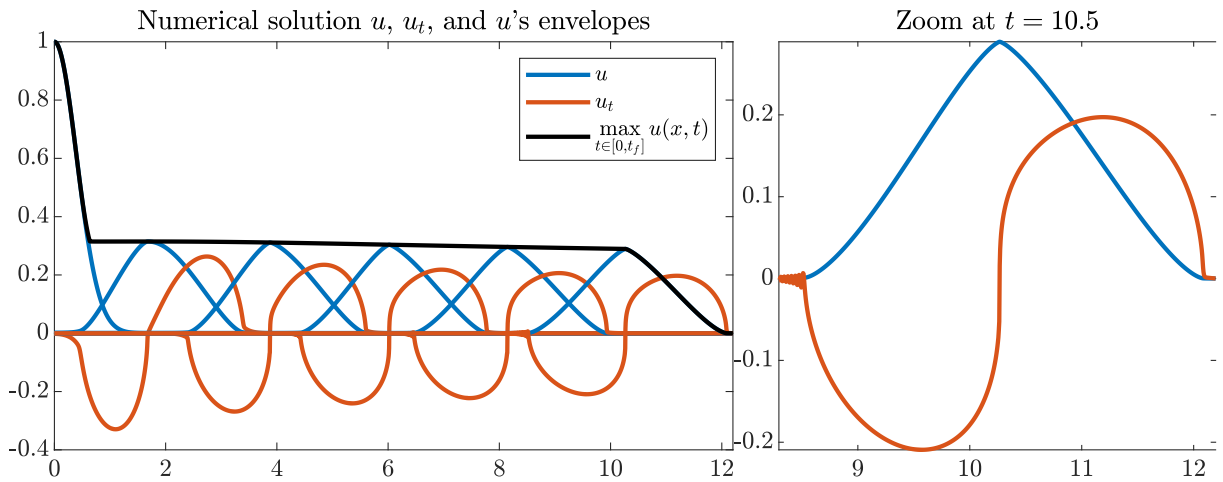


**Figure 7.2:** Left: the dynamics of the numerical solution  $u(x, t)$  and  $u_t(x, t)$  of equation (7.2) for various  $t$ . Initially there is a Gaussian explosion at  $x = 0$ , after which the system splits into symmetric left- and right-travelling waves; only the right half is shown. The  $u$  envelope is plotted in black. Right: A zoomed-in plot of the final values of  $u$  and  $u_t$ .

The numerical solution quickly evolves to look like a bounded version of equation (7.5) (where  $u_{tx}$  is unbounded at the maximum of  $u$ ).

The shape in the numerical solution in Figure 7.2 is rather stable. To demonstrate its stability, we re-solved the above problem on a domain with periodic boundary conditions, took the time span long enough for the wave to collide with itself twice, and plotted the results in Figure 7.3. The nonlinear and dispersive effects are much less apparent over time as the wave amplitude decreases, effectively switching the system into the linear mode.

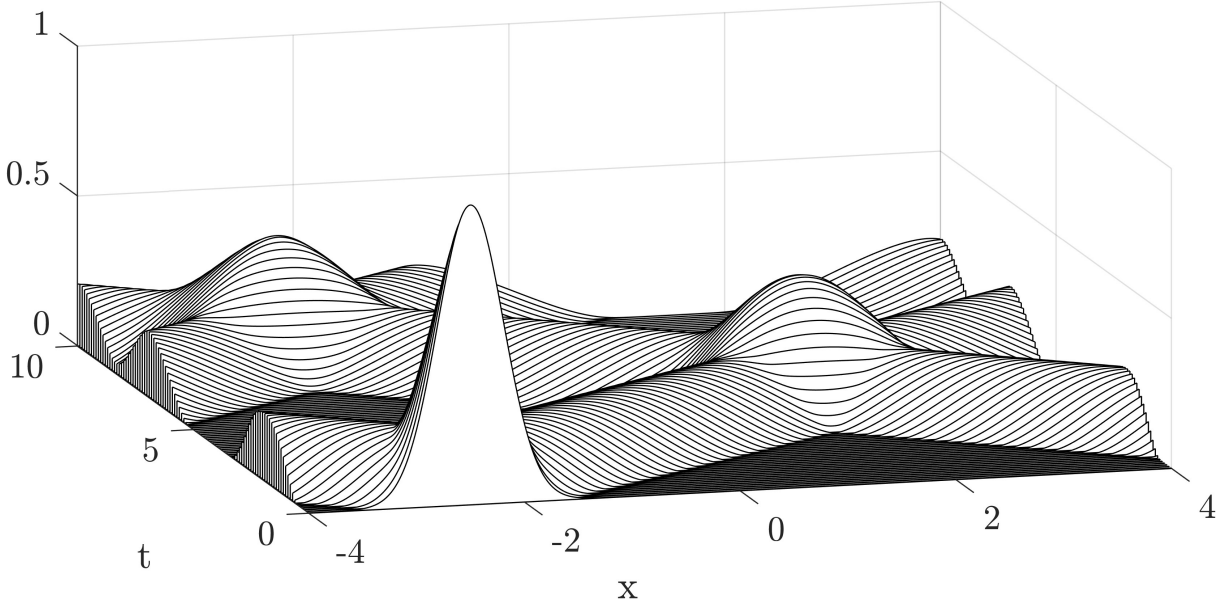


**Figure 7.3:** The travelling wave amplitude  $u(x, t)$  in a domain with periodic boundary conditions for an initial Gaussian explosion  $u(x, 0) = e^{-\ln(100)(x^2+2.5)/0.85^2}$ .

We note that it is possible to construct a bounded continuously differentiable piecewise function as a combination of the symmetry invariant solutions (7.5) taking, for example,

$$(F'(x))^3 = a \begin{cases} e^{-x} - 1 & \text{if } 0 \leq x \leq b, \\ (1 - e^b)e^{-x} & \text{if } b < x, \\ -(F'(-x))^3 & \text{otherwise.} \end{cases}$$

Though this formula does not yield a travelling wave solution itself, it produces a well-behaved wave when used as an initial condition for the PDE (7.2) along with the time derivative condition  $u_t(x, t) = -cF'(x)$ . The numerical solution is plotted in Figure 7.4 along with the wave's envelope.

## 8 Discussion

Waves travelling on interfaces between materials with different mechanical properties, such as Love waves in geological sciences, are an important object of study due to their unique propagation properties. In this paper, hyperelasticity and hyper-viscoelasticity frameworks were used to derive equations for shear displacements in the  $Y$ -direction propagating in  $(X, Z)$ -plane, holding for an arbitrary hyperelastic potential (equation (4.9)). With these frameworks, the linear wave equations for the Love wave model of interfacial waves was generalized to the nonlinear case, in particular, for the cubic Yeoh constitutive model (3.11) (equation (4.10)).

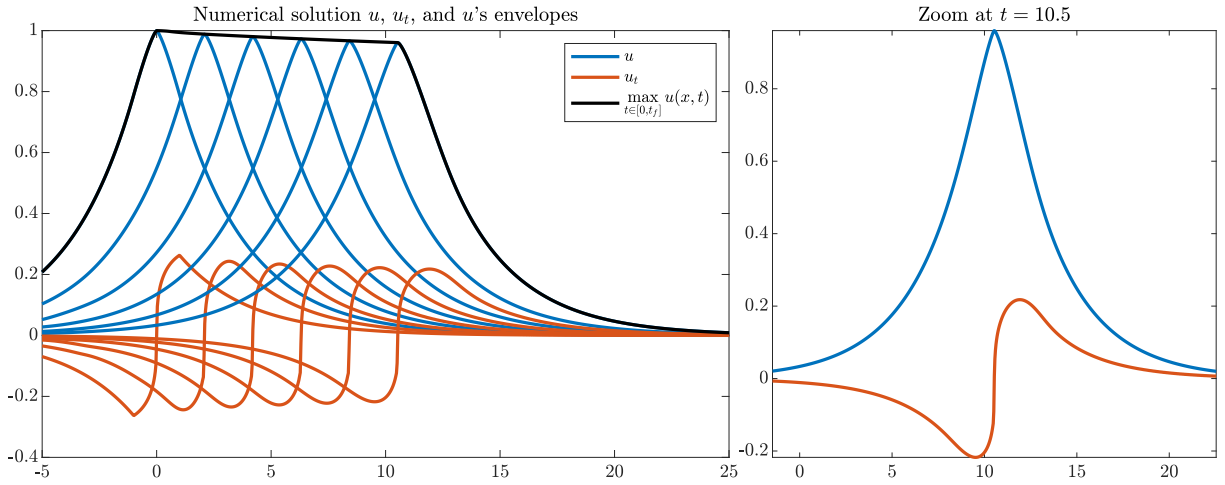


**Figure 7.4:** Left: plots of the solutions  $u(x, t)$  and  $u_t(x, t)$  of equation (7.2) for various  $t$ . The initial condition is a piecewise continuously differentiable function whose pieces are of the form (7.5). Initially,  $u_t$  is not differentiable at the breakpoints, but smooths out as the simulation progresses.

In the context of fiber-reinforced anisotropic solids, it has been previously shown that one-dimensional nonlinear waves of the form (4.11) with purely quadratic nonlinearity ( $A = 0$ ) led to wave breaking [9], which was eliminated when a viscosity term was taken into account. In this work, viscoelastic effects in one and two spatial dimensions were described through the pseudopotential (5.4) and the corresponding the viscoelastic stress (5.2).

Nonlinear Love-type waves propagating along the contact of two solid media (Figure 2.1) satisfying the Love wave existence condition  $c_1 < |v| < c_2$  (1.2) and the linear Hookean, nonlinear hyperelastic, and nonlinear hyper-viscoelastic equations were studied using the numerical method of lines in two spatial dimensions (Section 6). Interfacial waves on the contact of the two media and surface waves at the free surface of the top domain were tracked and their speeds were determined; in agreement with the linear Love wave theory, it was found that the phase velocity of the nonlinear Love waves satisfied the condition (1.2), with the phase velocity approaching the larger of the two material velocities  $c_2$  (Figures 6.5–6.18).

For a one-dimensional reduction, the nonlinear wave equations (7.1) in hyper-viscoelastic settings were studied using the point symmetry analysis. The linear combination of symmetries (7.3) yielded an invariant solution of a physical wave shape; however, that solution was unbounded. Numerical simulations with appropriate initial conditions demonstrated a qualitative agreement of numerical and exact solutions, in particular, the propagation of a wave with approximately constant speed and an amplitude decaying due to viscous effects.

Future work may include the study of anisotropic effects of Love-type wave behaviour through the use of more general hyperelastic constitutive laws with additional anisotropy terms (e.g., [9, 30] and references therein). It is also of interest to apply hyperelasticity theory to derive and study nonlinear generalizations of equations for other (compressional) surface waves, including Rayleigh waves that propagate along the free surface between a vacuum overlaying a solid, Scholte waves that move along fluid-solid interfaces, and Stoneley waves that propagate along the interface between two elastic solids. The analysis of such waves is complicated by the need to use compressible hyperelasticity, which employs a different set of strain tensor invariants and results in significantly more complex equations of motion.

## Acknowledgements

S.M. and S.A. thank the Department of Mathematics and Statistics, University of Saskatchewan for the support throughout the Master’s thesis program. S.M. and A.C. are grateful to NSERC of Canada for research support through a CGS-M grant and a Discovery grant RGPIN-2024-04308.

## Addendum

The original version of this paper contains an error in Subsection 4.1, where we substituted the result  $I_1 = I_2 = v_X^2 + v_Z^2 + 3$  into the strain energy density function before expanding the formula for the Piola-Kirchoff tensor  $\mathbf{P}$  in (3.3). In effect, we implicitly assumed that  $W_2^H = 0$ , neglecting the compatibility condition (4.6) necessary to ensure the hydrostatic pressure  $p$  is well defined when  $W_2^H \neq 0$ . This led to some minor errors in other examples. These issues are remedied by explicitly stating our focus on generalized neo-Hookean materials. These are materials where the strain energy density function  $W^H$  does not depend on the second invariant:  $W_2^H = 0$ . This error led to some other minor errors throughout which are now corrected. Because of our restriction to generalized neo-Hookean materials, any discussion around the Murnaghan model was replaced with the cubic Yeoh model. There was one other minor error in the caption of Figure 7.3, which is now corrected. The remainder of the paper stands without issue.

Since publishing, we discovered numerically breaking wave solutions, which we include as an appendix. The numbering for each section, figure, and equation was adjusted to include this work as a chapter in this thesis.

## A A comment on radially symmetric wave solutions that break numerically

At the time of publishing, the authors had not observed numerically breaking wave solutions of the PDE

$$u_{tt} = \nabla \cdot (W'(u_X^2 + u_Z^2)\nabla u). \quad (\text{A.1})$$

Equation (A.1) is (4.5b) with each constant absorbed into  $W$ . Since then, we discovered that it is possible for such solutions to break numerically. To study these solutions at a high resolution, we assert that the initial conditions and domain are radially symmetric. This assertion results in the (1 + 1)-dimensional PDE

$$ru_{tt} = (rW'(u_r^2)u_r)_r, \quad (\text{A.2})$$

where  $r$  is the radius from the point of symmetry. Taking  $W'(I_1) = a + \epsilon I_1$  yields the equation

$$ru_{tt} = (r(u_r + \epsilon u_r^3/3))_r, \quad u_r(0, t) = 0, \quad u(\infty, t) = 0 \quad (\text{A.3})$$

Figure A.1 plots profiles of (A.3) at various times as computed numerically via the method of lines with initial conditions  $u(r, 0) = e^{-r^2}$ ,  $u_t(r, 0) = -\frac{d}{dr}u(r, 0)$ , and  $\epsilon = 1$ . For this mesh, spurious oscillations form in  $u_r$  as early as  $t = 6.8$ , and begin to alter the envelope of  $u_r$  around  $t = 7.5$ . These oscillations are typical for numerically breaking waves. The solution  $u$  itself remains continuous, but a sudden change in its slope is evident around  $t = 8.3$  and  $r = 10$ . After the wave passes, the material remains displaced by at least 0.1 for all simulation times and appears to gradually return to its initial configuration.

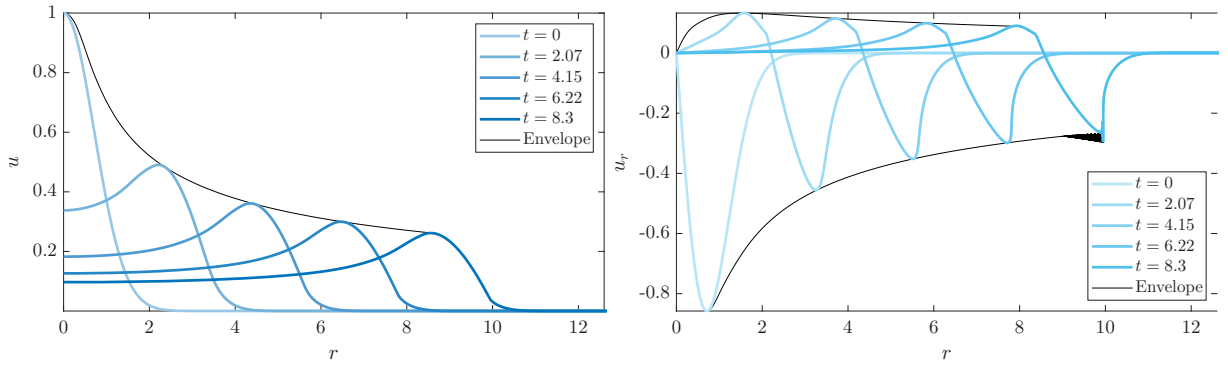


**Figure A.1:** Profiles of a numerical solution of (A.2) (left) and its spatial derivative  $u_r$  (right) at various times as computed via the method of lines for  $u(r, 0) = e^{-r^2}$ ,  $u_t(r, 0) = -\frac{d}{dr}u(r, 0)$ ,  $W'(I_1) = a + \epsilon I_1$ , and  $\epsilon = 1$ . The numerical domain is  $[0, 12.6]$  discretized by a uniform mesh of step size  $h = 0.00105$ .

To compare against another method of reducing the equation’s dimension, assume  $u_Z = 0$  in (A.1) to see

$$u_{tt} = (W'(u_X^2)u_X)_X. \quad (\text{A.4})$$

Symbolically, this equation is similar to (A.2), but solutions of these two equations behave very differently. For example, the boundary conditions are different and (A.4) is missing a factor of the independent variable  $X$ . Taking  $W'(I_1) = a + \epsilon I_1$  yields the equation

$$u_{tt} = (u_X + \epsilon u_X^3/3)_X. \quad (\text{A.5})$$

The spatial derivative  $u_X$  forms a jump discontinuity around  $t = 1.507$  for the same initial conditions and  $\epsilon = 1$ . It appears that solutions to (A.5) typically break sooner than those of (A.3).

## References

- [1] G. Marckmann and E. Verron, “Comparison of hyperelastic models for rubber-like materials,” *Rubber Chemistry and Technology*, vol. 79, no. 5, pp. 835–858, 2006.
- [2] L. Treloar, *The Physics of Rubber Elasticity*. Oxford University Press, 1975.
- [3] R. W. Ogden, “Large deformation isotropic elasticity—on the correlation of theory and experiment for incompressible rubberlike solids,” *Proceedings of the Royal Society of London. A. Mathematical and Physical Sciences*, vol. 326, no. 1567, pp. 565–584, 1972.
- [4] D. P. Pioletti and L. R. Rakotomanana, “Non-linear viscoelastic laws for soft biological tissues,” *European Journal of Mechanics-A/Solids*, vol. 19, no. 5, pp. 749–759, 2000.
- [5] A. Schettino, *Quantitative Plate Tectonics: Physics of the Earth – Plate Kinematics – Geodynamics*. Cham: Springer International Publishing, 2015.
- [6] F. D. Murnaghan, *Finite Deformation of an Elastic Solid*. Wiley, 1951.
- [7] D. R. Bland, *Nonlinear Dynamic Elasticity*. Blaisdell Publishing Company, 1969.
- [8] K. Bataille and F. Lund, “Nonlinear waves in elastic media,” *Physica D: Nonlinear Phenomena*, vol. 6, no. 1, pp. 95–104, 1982.
- [9] A. F. Cheviakov and J.-F. Ganghoffer, “One-dimensional nonlinear elastodynamic models and their local conservation laws with applications to biological membranes,” *Journal of the Mechanical Behavior of Biomedical Materials*, vol. 58, pp. 105–121, 2016.
- [10] K. F. Graff, *Wave Motion in Elastic Solids*. Courier Corporation, 2012.
- [11] P. G. Ciarlet, *Mathematical Elasticity. Volume 1: Three-dimensional Elasticity*, vol. 20 of *Studies in Mathematics and its Applications*. Amsterdam: Elsevier, 1988.

- [12] J. E. Marsden and T. J. R. Hughes, *Mathematical Foundations of Elasticity*. Dover, 1994.
- [13] A. F. Bower, *Applied Mechanics of Solids*. CRC press, 2009.
- [14] M. B. Boubaker, *Contribution mécanique à la réduction des marges en radiothérapie de la prostate: modélisation et simulation numérique du mouvement et de la déformation des organes pelviens*. PhD thesis, Institut National Polytechnique de Lorraine, 2009.
- [15] S. Hartmann, “Parameter estimation of hyperelasticity relations of generalized polynomial-type with constraint conditions,” *International Journal of Solids and Structures*, vol. 38, no. 44-45, pp. 7999–8018, 2001.
- [16] A. Nobili, “A weakly nonlinear Love hypothesis for longitudinal waves in elastic rods,” *International Journal of Non-Linear Mechanics*, vol. 163, p. 104737, 2024.
- [17] O. H. Yeoh, “Some forms of the strain energy function for rubber,” *Rubber Chemistry and technology*, vol. 66, no. 5, pp. 754–771, 1993.
- [18] S. O. Agyemang, “Shear Wave Models in Linear and Nonlinear Elastic Materials,” Master’s thesis, University of Saskatchewan, Saskatoon, Canada, 2020.
- [19] A. F. Cheviakov and J.-F. Ganghoffer, “Symmetry properties of two-dimensional Ciarlet–Mooney–Rivlin constitutive models in nonlinear elastodynamics,” *Journal of Mathematical Analysis and Applications*, vol. 396, no. 2, pp. 625–639, 2012.
- [20] N. Kambouchev, J. Fernandez, and R. Radovitzky, “A polyconvex model for materials with cubic symmetry,” *Modelling and Simulation in Materials Science and Engineering*, vol. 15, no. 5, p. 451, 2007.
- [21] E. Pucci and G. Saccomandi, “The anti-plane shear problem in nonlinear elasticity revisited,” *Journal of Elasticity*, vol. 113, no. 2, pp. 167–177, 2013.
- [22] C. Suchocki and S. Jemioło, “Polyconvex hyperelastic modeling of rubberlike materials,” *Journal of the Brazilian Society of Mechanical Sciences and Engineering*, vol. 43, no. 7, p. 352, 2021.
- [23] N. Kalyansaundaram, “Finite-amplitude Love-waves on an isotropic layered half-space,” *International Journal of Engineering Science*, vol. 19, no. 2, pp. 287–293, 1981.
- [24] M. Teymur, “Nonlinear modulation of Love waves in a compressible hyperelastic layered half space,” *International Journal of Engineering Science*, vol. 26, no. 9, pp. 907–927, 1988.
- [25] J. J. Rushchitsky, “On a nonlinear description of Love waves,” *International Applied Mechanics*, vol. 49, no. 6, pp. 629–640, 2013.
- [26] J. J. Rushchitsky, *Nonlinear Elastic Waves in Materials*. Springer, 2014.
- [27] G. A. Holzapfel, *Nonlinear Solid Mechanics: A Continuum Approach for Engineering*. Chichester, England: Wiley and Sons, 2000.
- [28] A. F. Cheviakov, “GeM software package for computation of symmetries and conservation laws of differential equations,” *Computer Physics Communications*, vol. 176, no. 1, pp. 48–61, 2007.
- [29] A. F. Cheviakov, “Symbolic computation of local symmetries of nonlinear and linear partial and ordinary differential equations,” *Mathematics in Computer Science*, vol. 4, no. 2-3, pp. 203–222, 2010.
- [30] A. Cheviakov, C. Lee, and R. Naz, “Radial waves in fiber-reinforced axially symmetric hyperelastic media,” *Communications in Nonlinear Science and Numerical Simulation*, vol. 95, p. 105649, 2021.